First-principles electronic structure calculations and topology analysis for anomalous Hall effect in the non-collinear antiferromagnets Mn_3AN

VU THI NGOC HUYEN

SEPTEMBER 2019

First-principles electronic structure calculations and topology analysis for anomalous Hall effect in the non-collinear antiferromagnets Mn_3AN

A dissertation submitted to

THE GRADUATE SCHOOL OF ENGINEERING SCIENCE
OSAKA UNIVERSITY

in partial fulfillment of the requirements for the degree of
DOCTOR OF PHILOSOPHY IN SCIENCE

BY

VU THI NGOC HUYEN

SEPTEMBER 2019

Abstract

Anomalous Hall (AH) effect has been known as an important macroscopic phenomenon in materials science because of its application in spintronics such as electronic probes, switches, and memory devices. The discovery of large AH effect in non-collinear antiferromagnets with no net magnetization leading an increasing amount of attention in studying the topological features of electronic band structure for the AH effect because of the insensitivity against an applied magnetic field and no stray fields interfering with the neighboring cells as well as faster spin dynamics than ferromagnets. This thesis aims to get a comprehensive understanding for AH effect by investigating topological features of electronic structures which produce large AH effect in the non-collinear antiferromagnetic metallic states of anti-perovskite manganese nitrides Mn_3AN(A= Ni, Cu, Ga, Ge, In, Sn, Ir) by first-principles density-functional-theory calculations. Firstly, the stable magnetic structures of these compounds are predicted to be non-collinear antiferromagnetic structures characterized by either T_{1g} or T_{2g} irreducible representation by evaluating the total energy for all of the magnetic structures classified according to the symmetry and multipole moments. Secondly, systematic evaluation of the AH conductivity leads to understanding the chemical trends of band filling and spin-orbit coupling in the series of materials. In order to understand the microscopic mechanism of the AH conductivity in a non-collinear magnetic system, the topology analysis is next performed for the Wannier based tight-binding models obtained from the first-principles calculations. This study reveals that the small Berry curvature which is widely spread around the Fermi surface in the Brillouin zone, dominantly contributes after the $\boldsymbol{k}$-space integration to the AH conductivity. While the locally divergent Berry curvature around Weyl points has a rather small contribution to the AH conductivity.

Contents

List of Figures

Chapter 1

Introduction

"The science of today is the technology of tomorrow."

Edward Teller

1.1 Anomalous Hall effect: a macroscopic transport phenomenon

One hundred forty years ago, Edwin Hall discovered the existence of a voltage difference in a conductor, transverse to the electric current and the external applied magnetic field perpendicular to the current as shown in Fig. 1.1 (a), and especially the effect in ferromagnet iron was found to be ten times larger than in non-magnetic conductor [1, 2]. The effect, which is called Hall effect, can be explained by a Lorentz force which pulls electrons to one side of the conductor. The experiments in 1930 and 1932 proposed a relation between Hall resistivity ρ_{xy} with applied perpendicular magnetic field H_z, and magnetization M_z in ferromagnets:

$$\rho_{xy} = R_0 H_z + R_s M_z, \tag{1.1}$$

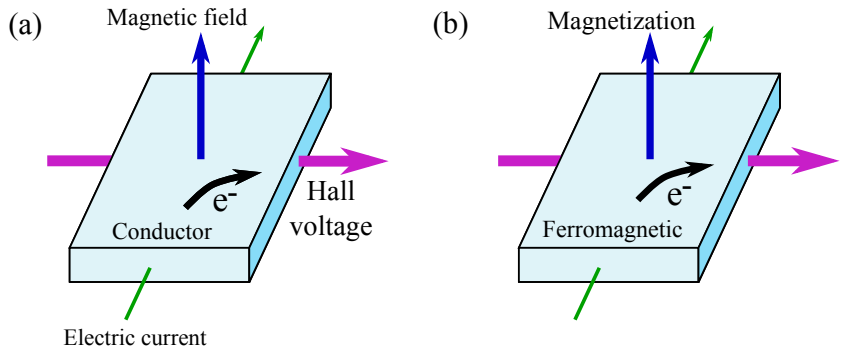

Figure 1.1: Schematic illustration of the Hall effect in an electrical conductor (a) and the anomalous Hall effect in a ferromagnet (b). The symbol e^- represents the electron with a negative electric charge.

where R_0 is a coefficient which related only to density of carriers and R_s depends on various properties of materials. The experiments also showed that even no external magnetic field, there was still a strong conductivity with only its inherent magnetization as shown in Fig. 1.1 (b). The effect is called "anomalous Hall (AH) effect" or sometimes called "extraordinary Hall effect". The AH effect is the electronic-magnetic phenomenon which has a large amount of attention with new recent exciting discoveries [3–12]. The AH effect in ferromagnets was widely applied for spintronic applications where electron spin is used to control and store information, instead of charge.

In general, the AH effect is also affected by scattering by impurities or disorders [13, 14]. In this work, we consider the AH effect that is independent of scattering, it is called intrinsic AH effect. In order to study the intrinsic AH effect which depends only on the band structure of the perfect crystal, first-principle density-functional-theory method is effective and convenient. The solution of the density-functional-calculation for an electron in periodic crystal are Bloch states [15] with eigenvalues $\epsilon(\boldsymbol{k})$ and wavefunctions (Bloch functions) $\psi(\boldsymbol{k}) = u_{n\boldsymbol{k}} e^{i\boldsymbol{k}\cdot\boldsymbol{r}}$ dependent on position in reciprocal space $\boldsymbol{k}$, where $u_{n\boldsymbol{k}}$ is the periodic part of Bloch function and $\boldsymbol{r}$ is the electron coordinate.

1.2 Topological aspects of the anomalous Hall effect

The AH effect was the "anomalous" matter which could not be explained clearly for a long time. Until when its topological aspects were considered, understanding about the macroscopic mechanism of the AH effect was effectively brought out. This concepts has a relation with electrostatic through Gauss's Law and Stock's theorem which describe properties of vector field $\boldsymbol{A}$ [16]. Stokes' theorem says:

$$\oint_C \boldsymbol{A} \cdot d\boldsymbol{l} = \int_S (\nabla \times \boldsymbol{A}) \cdot \boldsymbol{n} dS, \tag{1.2}$$

where S is an arbitrary open surface with the normal vector $\boldsymbol{n}$ and C is the closed curve surround S. The curl of the vector field $\nabla \times \boldsymbol{A}$ is so-called vector potential. These electrostatic concepts will be mentioned below to introduce the topological aspects.

The basic idea is that considering the AH effect is a cyclic adiabatic process. The phase change under the processes like that is called Berry phase:

$$\phi_n(C) = \oint_C d\boldsymbol{k} \cdot \boldsymbol{A}_n(\boldsymbol{k}), \tag{1.3}$$

where $\boldsymbol{A}_n(\boldsymbol{k})$ is $\boldsymbol{k}$ space Berry connection of band with index n, and is defined in term of the periodic part of Bloch function $u_{n\boldsymbol{k}}$ as follows:

$$\boldsymbol{A}_n(\boldsymbol{k}) = i \left\langle u_{n\boldsymbol{k}} | \nabla_{\boldsymbol{k}} u_{n\boldsymbol{k}} \right\rangle . \tag{1.4}$$

Berry curvature $\Omega_n(\boldsymbol{k})$ then is defined as the curl of the connection:

$$\Omega_n(\boldsymbol{k}) = \nabla_{\boldsymbol{k}} \times \boldsymbol{A}_n(\boldsymbol{k}) = \partial_\alpha A_\beta - \partial_\beta A_\alpha, \tag{1.5}$$

This adiabatic process is similar to a process when an electron moves in the periodic potential of a solid under perturbations such as weak electric and magnetic fields, its velocity has an extra term named "anomalous velocity" [17–21]:

$$\dot{\boldsymbol{r}} = \frac{1}{\hbar} \frac{\partial \epsilon_n(\boldsymbol{k})}{\partial \boldsymbol{k}} - \dot{\boldsymbol{k}} \times \Omega_n(\boldsymbol{k}), \tag{1.6}$$

where $\epsilon_n(\boldsymbol{k})$ is the eigenvalue of Bloch state. The AH conductivity in this theory is calculated by the Brillouin zone integration of the Berry curvature with the summation of the one-electron bands below the Fermi level [22, 23]:

$$\sigma_{\alpha\beta} = -\frac{e^2}{\hbar}\int \frac{d\boldsymbol{k}}{(2\pi)^3}\sum_n f_n(\boldsymbol{k})\Omega_{n,\alpha\beta}(\boldsymbol{k}) \tag{1.7}$$

where $\alpha, \beta = x, y, z$ $(\alpha \neq \beta)$, and $f_n(\boldsymbol{k}) = \theta(\epsilon_n(\boldsymbol{k}) - \mu)$ is the occupation factor determined from the eigenvalue of Bloch states $\epsilon_n(\boldsymbol{k})$ and the Fermi energy μ.

Under the Berry curvature concept, each band is characterized by a topological integer called the Chern number which is the Berry-curvature flux through a closed oriented surface S in $\boldsymbol{k}$ space:

$$C_n(S) = \frac{1}{2\pi}\oint_S dS\hat{\mathbf{n}}\cdot\boldsymbol{\Omega}_n(\boldsymbol{k}), \tag{1.8}$$

and it is known as the "Chern's theorem". When the surface S surrounds a crossing point between bands n and $n+1$, the Chern number becomes 'chirality' of that point $\chi_{n\alpha}$, with α indicates the αth crossing point between bands n and $n+1$. If that chirality is an integer number unequal zero, the crossing point is called a Weyl point $W_{n\alpha}$. Especially, the like-Gauss's law $\nabla\cdot\boldsymbol{\Omega}_n = 0$ is correct for everywhere in $\boldsymbol{k}$ space except at Weyl points [24]:

$$\nabla\cdot\boldsymbol{\Omega}_n(\boldsymbol{k}) = 2\pi\sum_\alpha \chi_{n\alpha}\delta^3(\boldsymbol{k}-\boldsymbol{k}_{n\alpha}) - 2\pi\sum_\alpha \chi_{n-1,\alpha}\delta^3(\boldsymbol{k}-\boldsymbol{k}_{n-1,\alpha}). \tag{1.9}$$

It can be understood from the above equation that the Weyl point acts as a source or a sink of Berry flux in the lower band and upper band, respectively as shown in Fig. 1.2. Therefore, Berry curvature around Weyl point was often assumed to play important roles in the AH effect. Note that while Berry connection at $\boldsymbol{k}$ can be changed continuously by modifying the phase choice for the Bloch states around $\boldsymbol{k}$, the Berry curvature is fully gauge invariant and referred as a "topological" nature. Then the contents such as Berry curvature, Chern number, and Weyl point are regarded as topological aspects of the AH effect.

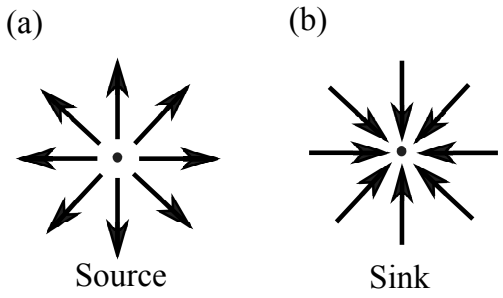

Figure 1.2: Schematic illustrations of Weyl points acting as a source (a) or a sink (b) of Berry curvature, the vectors indicates Berry curvature.

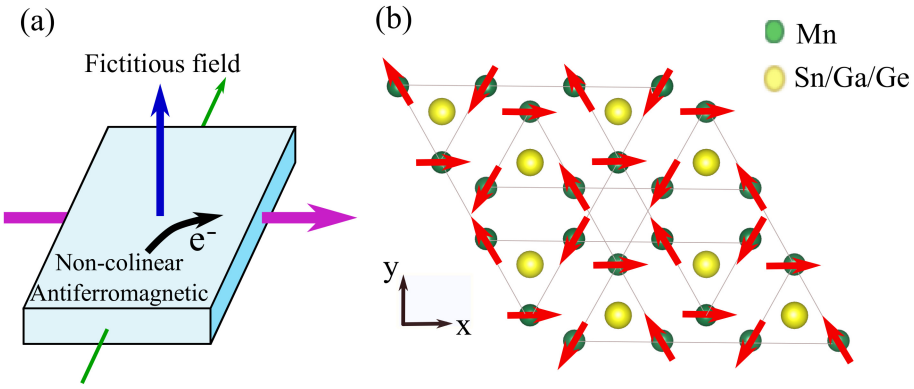

Figure 1.3: Schematic illustration of the anomalous Hall effect in non-collinear antiferromagnet (a) crystal and spin structure of Mn_3Z (Z= Sn, Ge, Ga) (b) with magnetic moments are sketched in red.

1.3 Anomalous Hall effect in non-collinear antiferromagnets

The AH effect was conventionally assumed proportional to the magnetization leading to no AH conductivity in antiferromagnets (AFM) with no net magnetization. Nevertheless, large AH effect was recently predicted by the first-principles calculations for non-collinear AFM with vanishing net magnetization [4–7]. It was first observed of large AH effect in a non-collinear AFM Mn_3Sn at room temperature

by Nakasuji *et al.* [8] in 2015. They proposed the fictitious field which drives the AH effect in antiferromagnetic instead of magnetization in ferromagnetic as shown in Fig. 1.3 (a). They found a residual in-plane magnetic moment in this Mn_3Sn. That tiny moment was then demonstrated in Ref. [10] to not contribute to induce the AH conductivity but to control the chirality of spin triangular structure shown in Fig. 1.3 (b). The large AH effect in AFM states has attracted an increasing amount of attention because of the insensitivity against an applied magnetic field and no stray fields interfering with the neighboring cells as well as faster spin dynamics than ferromagnets [8, 9, 25, 26]. Those findings of the AH effect in the non-collinear AFM states urge us to get a comprehensive understanding of possible AH effect in various magnetic states.

In general, the presence of AH effect in magnetic states is determined by symmetry of their Berry curvature or their magnetic symmetry that will be reminded in Appendix A. Recently, it has been proposed in Ref. [12] another approach called "cluster multipole (CMP) theory". The theory defines CMP moment being the multipole moment in the magnetic structure in analogous to the local multipole moments for an atom [27–29]. the CMP then can be characterized for the AH effect in arbitrary magnetic ordering including AFM structures. In addition, multipole expansion for magnetic structures was introduced to generate magnetic structures then classify them into multipoles [30, 31]. The summary of the CMP theory along with multipole expansion for magnetic structure will be explained in Appendix B.

In particular, the CMP identifies the order parameters which induce the AH effect as a nature extensive of magnetization in ferromagnets. The theory says that an arbitrary magnetic order can induce the AH effect by breaking the magnetic symmetry same as that for ordinary ferromagnetic order. The cluster multipole theory, therefore, is useful to generate and classify magnetic structures as well as determine structures including AFM states can induce finite AH conductivity effectively.

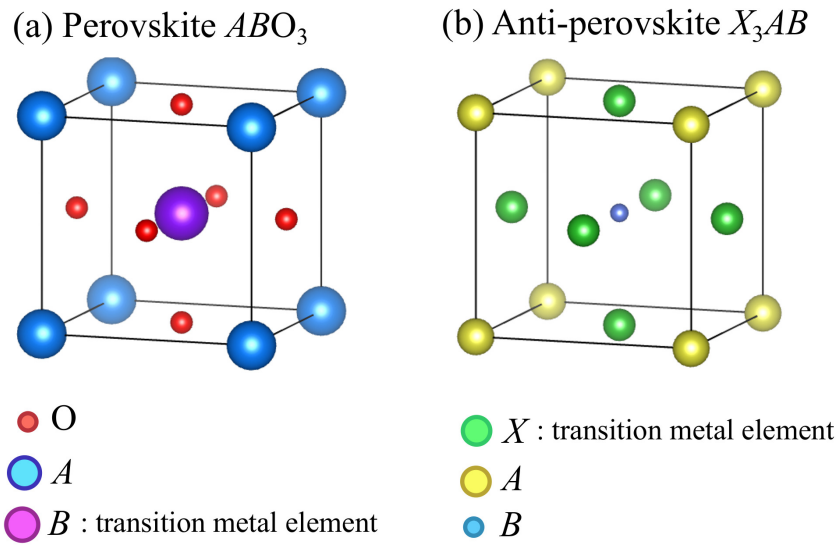

Figure 1.4: Crystal structures of perovskite (a) and anti-perovskite (b), respectively.

1.4 Anti-perovskite manganese nitrides Mn_3AN

It will be shown here properties and advantages of anti-perovskite manganese nitrides for studying the AH effect in non-collinear antiferromagnetic systems. Figure 1.4 is to introduce crystal structures of perovskite and anti-perovskite systems. They both have a cubic structure with general formula of ABO_3 for perovskite and X_3AB for anti-perovskite. In a unit cell, perovskite has only one transition metal element at body-cubic center. In contract, anti-perovskite has three transition metal elements at face-cubic centers. Many perovskites are known to be insulators. Therein, the name perovskite was firstly called for $CaTiO_3$ with little application [32], the later similar structures known such as $BaTiO_3$ and $PbZrO_3$ are ferroelectricity *i.e.* having a spontaneous electric polarization [33,34].

The increasing number of transition metal elements in a unit cell leading to exhibiting more some interesting features in anti-perovskites. For example, some anti-perovskites such as Li_3OBr, Li_3OCl, and Na_3OCl show high conductivity which can be used for batteries and sensors [35,36]. Their properties such as good

electrical conductor and magnetism were shown mainly related to d-orbital of transition metal elements [37]. There are also many famous anti-perovskites being metallic with B representing B, C, or N element; X being a magnetic element, Mn, Ni or Fe while A being a non-magnetic element, Cu, Zn, Ga, Cd, and Sn. They exhibit superconductivity, giant magnetoresistance, thermal expansion, and some rare properties such as giant baro-caloric effect in Mn_3GaN and magneto-caloric effect in Mn_3SnC and Mn_3GaC which are useful for magnetic refrigeration [38].

Especially, among them anti-perovskite manganese nitrides Mn_3AN (A= Ni, Sn) were found to show non-collinear AFM in the triangular Mn lattice corresponding to irreducible representations $T_{1g}(\Gamma_4^+)$ and $T_{2g}(\Gamma_5^+)$, respectively [39–41] as shown in Fig. 1.5. A recent study on spin-order dependent AH effect in the non-collinear AFM Mn_3AN (A= Ga, Zn, Ag, or Ni) also suggested that these material are an excellent AFM platform for realizing novel spintronics applications [42]. In this context, they can be regarded as a new playground to explore the AH effect in antiferromagnetic with many analogues to replace nonmagnetic elements A.

1.5 Motivation and overview of the thesis

1.5.1 Motivation

In ferromagnetic states, there were many theoretical and experimental works focused on exploring the relation between the topological feature of electronic band structures [3]. In particular, the AH effect was suggested mainly arising from large Berry curvature around the Weyl points in Weyl semimetals [43,44]. For metallic ferromagnetic bcc-Fe, Martínez *et al.* investigated topological feature related to the AH effect and found the dominant contribution from the Berry curvature distribution across the Fermi sheets with the possible enhanced contribution from the Fermi sheets having the Weyl points very nearby [24]. In non-collinear AFM Mn_3Ge and Mn_3Sn, it was observed multiple Weyl points which can give large

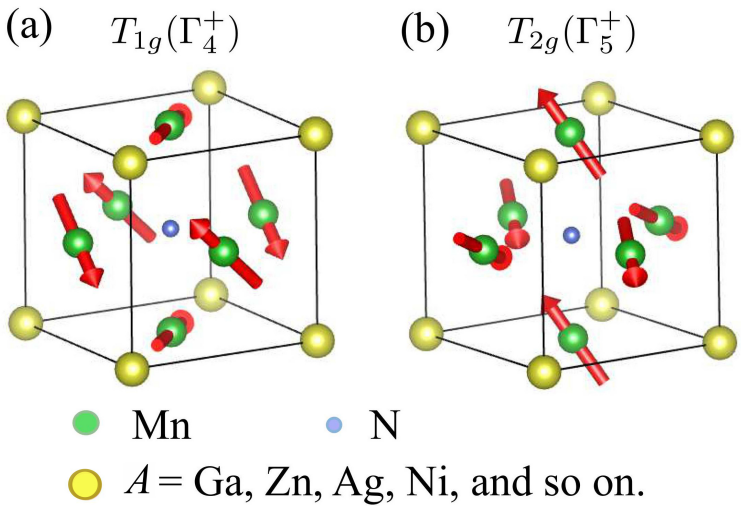

Figure 1.5: Crystal structures of anti-perovskite manganese nitrides in corresponding to irreducible representations $T_{1g}(\Gamma_4^+)$ (a) and $T_{2g}(\Gamma_5^+)$ (b), respectively. Mn, non-magnetic atom A, and N atoms are located at the face center, corner, center of the cubic unit cell, respectively.

influence to the AH effect [11]. Nevertheless, topological aspects of the AH effect in non-collinear AFM Mn_3AN have not been investigated. Therefore this thesis aims to identify important factors for the large AH effect by detailed analysis of topological aspects including Weyl points, Berry curvature, and Fermi surfaces in the platform of Mn_3AN.

1.5.2 Overview

This thesis analyzes the magnetic structures classified according to symmetry and cluster multipoles and find that non-collinear antiferromagnetic structures characterized by higher rank multipoles are stabilized in those compounds. Symmetry analysis reveals that the AH effect can emerge in the magnetic configurations characterized by T_{1g} irreducible representation that the magnetic dipole ordering belongs to. The results of systematic analysis for the AH effect in anti-perovskite

manganese nitrides Mn_3AN (A= Ni, Cu, Zn, Ga, Ge, Pd, In, Sn, Ir, Pt) are provided along with discussion the stability, symmetry, and topological aspects of the magnetic structures leading to the AH effect.

In particular, this thesis identifies important factors for the large AH effect with the detailed analysis of Weyl points, Berry curvature, and Fermi surfaces, which characterize the topological features of the magnetic systems, by means of first-principle density-functional-theory calculations. The thesis finds that the AH effect is dominantly contributed from the Berry curvatures widely spread around the Fermi surfaces induced with the band splitting due to the spin-orbit coupling and the contribution from the divergent Berry curvature, for instance, around Weyl points is rather small.

This thesis is organized as follows. Chapter 2 presents methods of calculation including density functional theory to obtain ground states with eigenvalues and Bloch functions and Wannier function method to evaluate the AH conductivity. Therein, the fundamental equation of quantum mechanics named the Kohn-Sham equation is introduced. The solving method to deal with problems of the Kohn-Sham equation such as treating potential, choosing basis sets, dealing with spin-polarized systems, and treating of relativistic effect of electrons.

Results and discussion are presented in Chap. 3. It is firstly provided a symmetry analysis related to the AH effect in Mn_3AN. Then the chapter present the result of the stability of magnetic ordering in these compounds which mentioned in the symmetry analysis. The general results for electronic of the AH conductivity in Mn_3AN including the calculated AH conductivity and discussion the basic mechanism for obtaining Berry curvature as well as different AH conductivities. The main results will be shown as a topology analysis of Weyl points, Berry curvature, and Fermi surface which related to topological aspects in the AH effect. Then the dominant factor that contributes to the AH conductivity is discussed in the last of the chapter. Finally, Chap. 4 gives the summary of this thesis.

Chapter 2

Methods

This chapter presents the basic concepts of two methods of calculation in this thesis. They are density functional theory and Wannier function method.

2.1 Density functional theory

This section introduces the fundamental equation of quantum mechanics named the Kohn-Sham equation. The solving method to deal with problems of the Kohn-Sham equation such as treating potential, choosing basis sets, dealing with spin-polarized systems, and treating of relativistic effect of electrons are mentioned.

2.1.1 Quantum many-body problem

Density functional theory (DFT) calculation is a standard tool for solving materials problems in many fields such as physics, chemistry, and materials science. Basically, this calculation aims to obtain the ground state density while other characteristics can be expressed through this density. The origin of this method comes from a basis problem in solid state named a quantum many-body problem, therein it is necessary to solve Schrödinger equation with many degrees of freedom

of N nuclei and ZN electrons:

$$\hat{H}\psi = E\psi, \tag{2.1}$$

where E is the total energy, ψ is the wave function, and $\hat{H}$ is the Hamiltonian operator written as follows:

$$\begin{aligned}\hat{H} = &-\frac{1}{2}\sum_i \frac{\nabla^2_{\boldsymbol{R}_i}}{M_i} - \frac{1}{2}\sum_i \frac{\nabla^2_{\boldsymbol{r}_i}}{m_e} \\ &- \sum_{i,j}\frac{e^2 Z_i}{|\boldsymbol{R}_i - \boldsymbol{r}_j|} + \sum_{i\neq j}\frac{e^2}{|\boldsymbol{r}_i - \boldsymbol{r}_j|} + \sum_{i\neq j}\frac{e^2 Z_i Z_j}{|\boldsymbol{R}_i - \boldsymbol{R}_j|},\end{aligned} \tag{2.2}$$

with the electrons are located at $\boldsymbol{r}_i$ and have mass m_e, the nucleus are located at $\boldsymbol{R}_i$ and have mass M_i. The first and second term are kinetic energy operator of nuclei and electrons, respectively. The interaction between electron and nuclei, between electrons and electrons, between nuclei and nuclei are expressed by the Coulomb interaction in the third, forth, and fifth terms, respectively. This equation can not be solved exactly and some approximations are necessary to be applied.

The Born-Oppernheimer approximation assumes that the nuclei are 'freeze' at fixed position because they are much heavier and slower than the electrons. The many-body problem now becomes a problem of many-electron in an 'external' potential of the nuclei. The kinetic term of nuclei in Eq. 2.2 disappears because the nuclei do not move any more, the Coulomb interaction nuclei-nuclei becomes a constant. There are left some following terms.

$$\hat{T} = -\frac{1}{2}\sum_i \frac{\nabla^2_{\boldsymbol{r}_i}}{m_e} \tag{2.3}$$

is the kinetic energy of the electron gas,

$$\hat{V}_{ext} = -\sum_{i,j}\frac{e^2 Z_i}{|\boldsymbol{R}_i - \boldsymbol{r}_j|} \tag{2.4}$$

is the potential energy of the electron in the 'external' potential of nuclei, and

$$\hat{V}_{ee} = \frac{1}{2}\sum_{i\neq j}\frac{e^2}{|\boldsymbol{r}_i - \boldsymbol{r}_j|} \tag{2.5}$$

is the potential energy due to electron-electron interactions. The Hamiltonian now write as:

$$\hat{H} = \hat{T} + \hat{V}_{ee} + \hat{V}_{ext}. \tag{2.6}$$

It is much simple than the problem in Eq. 2.2 but still can not be solved. Some approximations were proposed to simplify more Eq. 2.6 such as the Hatree-Fock method [45–48]. which is suitable for atoms and molecules in quantum chemistry. However, this method is less accurate for solid systems. Density functional theory, which is a more modern and appropriate method for solving the quantum many-body problem than early approximations.

2.1.2 Density functional theory

Hohenberg and Kohn theorem

Density functional theory (DFT) has been established in 1964 by Hohenberg and Kohn [49] with two basic theorems.

Theorem 1: *The total energy of the system is a unique functional of the density* $n(\boldsymbol{r})$*:*

$$E[n(\boldsymbol{r})] = T[n(\boldsymbol{r})] + V_{ext}[n(\boldsymbol{r})] + V_{ee}[n(\boldsymbol{r})]. \tag{2.7}$$

Theorem 2 : *The total energy functional* $E[n(r)]$ *is minimized for the exact ground-state density* $n_0(r)$ *under the constraint that the total number of electrons is kept fixed:*

$$E[n_0(\boldsymbol{r})] \leqslant E[n(\boldsymbol{r})]. \tag{2.8}$$

If the form of energy function $E[n(\boldsymbol{r})]$ is known, the electronic density and total energy of the ground state are able to obtain. Therefore, it is necessary to find an approximation for the energy functional.

Kohn-Sham equation

In 1965, Kohn and Sham proposed an equation that makes DFT to have a large amount of applications until nowadays. The total energy functional can be rewritten into four parts:

$$E[n] = T[n] + V_{ext}[n] + \int\int \frac{n(\boldsymbol{r})n(\boldsymbol{r}')}{|\boldsymbol{r}-\boldsymbol{r}'|}d\boldsymbol{r}d\boldsymbol{r}' + E_{xc}[n], \tag{2.9}$$

with the term $\int\int \frac{n(\boldsymbol{r})n(\boldsymbol{r}')}{|\boldsymbol{r}-\boldsymbol{r}'|}d\boldsymbol{r}d\boldsymbol{r}'$ and $E_{xc}[n]$ are the Hatree and the exchange-correlation energy. In this equation, both T and E_{xc} are not known. The kinetic term T can be splited into the kinetic energy of non-interacting particles which can determine from single-particle wave function $\psi_i(\boldsymbol{r})$ and T_{xc}. Then it turns to solve the N one-electron equations named Kohn-Sham equation:

$$\left[-\frac{1}{2}\bigtriangledown^2 + v_{\text{eff}}(\boldsymbol{r})\right]\psi_i(\boldsymbol{r}) = \epsilon_i\psi_i(\boldsymbol{r}), \tag{2.10}$$

where ϵ_i is eigenvalue, ψ_i is the corresponding wave function, and v_{eff} is called the effective potential, which can be separated into:

$$v_{\text{eff}}(\boldsymbol{r}) = v_{\text{ext}}(\boldsymbol{r}) + v_{\text{xc}}(\boldsymbol{r}) + \int \frac{n(\boldsymbol{r})}{|\boldsymbol{r}-\boldsymbol{r}'|}d\boldsymbol{r}', \tag{2.11}$$

with $v_{\text{xc}}(\boldsymbol{r}) = \frac{\delta(E_{xc}+T_{xc})}{\delta n(\boldsymbol{r})}$ is the exchange-correlation potential. In the followings, the T_{xc} is assumed including in the E_{xc}.

Including spin-polarization: The beginning content of DFT was introduced for non-magnetic system, but it can also be applied for spin-polarized system [50] by adding an external magnetic field $\boldsymbol{B}_{\text{ext}}$. The spin, or magnetization density $\boldsymbol{m}(\boldsymbol{r})$ is introduced with the vector Pauli matrices $\boldsymbol{\sigma}$ to construct the 2×2 electronic and magnetization density matrix $\rho(\boldsymbol{r}) = \frac{1}{2}[n(\boldsymbol{r})I + \boldsymbol{m}(\boldsymbol{r})\cdot\boldsymbol{\sigma}]$, where I is the 2×2 unit matrix. Now, the electric and magnetic density can be written as:

$$n(\boldsymbol{r}) = \sum_i \sum_{\alpha=\pm} |\psi_{i\alpha}(\boldsymbol{r})|^2, \tag{2.12}$$

$$m(\boldsymbol{r}) = \sum_i \boldsymbol{\psi}_i^\dagger(\boldsymbol{r})\boldsymbol{\sigma}\boldsymbol{\psi}_i(\boldsymbol{r}), \tag{2.13}$$

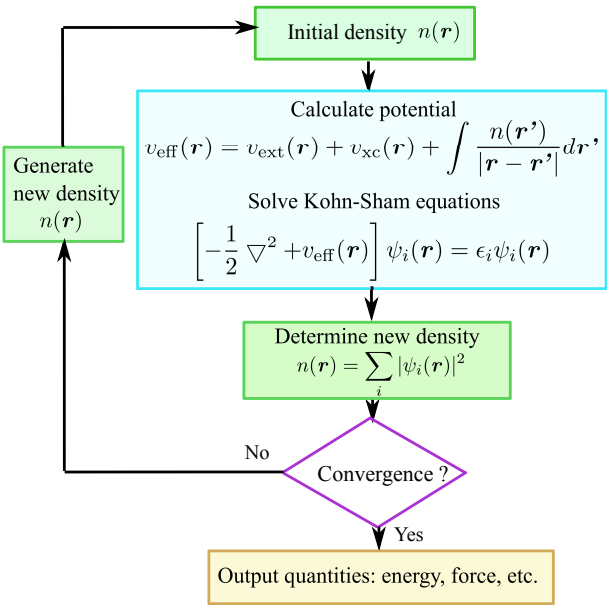

Figure 2.1: Self-consistency circle of density functional theory

where $\alpha = \pm$ for spin-up and down. The spin-polarized Kohn-Sham equation has a form:

$$\left[-\frac{1}{2}\nabla^2 + v_{\rm eff}(\boldsymbol{r}) + \boldsymbol{\sigma}\cdot\boldsymbol{B}_{\rm eff}\right]\boldsymbol{\psi}_i(\boldsymbol{r}) = \epsilon_i\boldsymbol{\psi}_i(\boldsymbol{r}), \tag{2.14}$$

where the effective magnetic field $\boldsymbol{B}_{\rm eff} = \boldsymbol{B}_{\rm ext} + \boldsymbol{B}_{\rm xc}$ contain the 'exchange' field arising from the exchange-correlation energy ϵ_{xc} as a function of electron density $n(\boldsymbol{r})$ and magnetization density $\boldsymbol{m}(\boldsymbol{r})$:

$$\boldsymbol{B}_{xc}(\boldsymbol{r}) = \frac{\partial\epsilon_{xc}(n(\boldsymbol{r}),\boldsymbol{m}(\boldsymbol{r}))}{\partial\boldsymbol{m}(\boldsymbol{r})}. \tag{2.15}$$

In the case of "collinear magnetism" $\boldsymbol{B}_{\rm eff}(\boldsymbol{r}) = B_{\rm eff}(\boldsymbol{r})\hat{\boldsymbol{e}}_z$, the wavefuntions of spin-up and spin-down electrons can be solved from the equations:

$$\begin{aligned}\left[-\frac{1}{2}\nabla^2 + v_{\rm eff}(\boldsymbol{r}) + B_{\rm eff}(\boldsymbol{r})\right]\psi_{i+}(\boldsymbol{r}) &= \epsilon_{i+}\psi_{i+}(\boldsymbol{r}),\\ \left[-\frac{1}{2}\nabla^2 + v_{\rm eff}(\boldsymbol{r}) - B_{\rm eff}(\boldsymbol{r})\right]\psi_{i-}(\boldsymbol{r}) &= \epsilon_{i-}\psi_{i-}(\boldsymbol{r}),\end{aligned} \tag{2.16}$$

and the densities of spin-up and spin-down are $n_+(\boldsymbol{r}) = \sum_i |\psi_{i+}(\boldsymbol{r})|^2$ and $n_-(\boldsymbol{r}) =$

$\sum_i |\psi_{i-}(\boldsymbol{r})|^2$, respectively. Then the electron density reads $n(\boldsymbol{r}) = n_+(\boldsymbol{r}) + n_-(\boldsymbol{r})$, and the corresponding magnetization density is $m(\boldsymbol{r}) = n_+(\boldsymbol{r}) - n_-(\boldsymbol{r})$.

Treating for non-collinear magnetism: In the approximation of non-collinear magnetism, it is necessary to define local spin-quantization axis $\hat{e}_\mu$ as the z-axis parallels to the direction of the local magnetic moment. The spin-quantization axis of each state can vary with position. In some cases, when non-ground state non-collinear magnetism systems is needed to consider, that means the direction of the magnetic moments is needed to be constrained. The constrained method introduce a penalty functional to the Hamiltonian [51–56].

However, this work aim to obtain the non-collinear magnetic configuration correspond to an energy minimum. Then only an initial magnetic ordering is needed to be set up. The magnetic states can automatically reach to a ground state spin order without any constrained approach to spin direction [57].

Including relativistic effects: When the relativistic effect is included in the Kohn-Sham equations, they are called the massive-one-particle Dirac equations [58]:

$$\left[c \sum_{i=1}^{3} \alpha_i p_i + (\beta - 1) m_0 c^2 + V_{\text{eff}}(\boldsymbol{r}) \right] \psi(\boldsymbol{r}) = E \psi(\boldsymbol{r}) \tag{2.17}$$

where c is the speed of light, m_0 is the electron's rest mass, p_i are its momentum ($i = x, y, z$). α_i and β are determined from 2×2 Pauli matrixes and the 2×2 unit matrix I:

$$\alpha_i = \begin{pmatrix} 0 & \sigma_i \\ \sigma_i & 0 \end{pmatrix}, \tag{2.18}$$

$$\beta = \begin{pmatrix} I & 0 \\ 0 & -I \end{pmatrix}. \tag{2.19}$$

where Pauli matrices are:

$$\sigma_1 = \begin{pmatrix} 0 & 1 \\ 1 & 0 \end{pmatrix}, \sigma_2 = \begin{pmatrix} 0 & -i \\ i & 0 \end{pmatrix}, \sigma_3 = \begin{pmatrix} 1 & 0 \\ 0 & -1 \end{pmatrix} \tag{2.20}$$

The eigenvectors are four-component wave functions. The equation including relativistic for mass-velocity, Darwin, and higher terms [58]. It is more complex than

a non-relativistic equation. There are some approximation methods to include the relativistic effect. For example, "scalar relativistic approximation" neglects the spin-orbit coupling (SOC) which was known as a relativistic effect caused by a coupling of the spin angular momentum (intrinsic magnetic moment) of the electron and the orbital angular momentum (magnetic field seen in its orbital motion around the nucleus). However, when a system contains heavy atoms with $4d$ and $5d$ electrons, the SOC is quite large and it is necessary to take into account the SOC effect. In that case, a "second-variation" procedure [59–63] is used to include SOC based on perturbation theory after obtaining the solution of the "scalar relativistic" equation.

Treatment of potential

The full-potential method uses full potential and charge density without any "shape" approximations in the interstitial region and inside the muffin tins. This method has a high accuracy for various systems. However, some "shape" approximations were applied to the effective potential for convention in some approaches. In that case, the potential is called pseudopotential. There is a kind of pseudopotential named "norm-conserving" proposed by Hamann, Schlüter, and Chiang [64,65]. In this pseudopotential, the pseudo-wave function ψ_{PP} must have the same norm as the all-electron wave function $\psi_{\mathrm{all-electron}}$:

$$\int_0^{r_c} |\psi_{\mathrm{PP}}(\boldsymbol{r})|^2 d\boldsymbol{r} = \int_0^{r_c} |\psi_{\mathrm{all-electron}}(\boldsymbol{r})|^2 d\boldsymbol{r} \tag{2.21}$$

within chosen core radius r_c. The region outside the core radius, the pseudo and all-electron wave function are identical. In general, the norm-conserving pseudopotentials were shown not good for $3d$-transition metals and rare-earth elements because of their strongly localized orbitals [64,65]. This problem was solved by the ultrasoft pseudopotentials proposed by Vanderbilt [66]. The idea of ultrasoft pseudopotential is to relax the norm conservation criteria to obtain smoother pseudo wave functions. Then it can be expanded with a smaller number of plane waves.

Exchange and correlation functional

Ground-state properties of any interacting many-electron system can be obtained if the exchange-correlation $E_{xc}[n(\boldsymbol{r}), \boldsymbol{m}(\boldsymbol{r})]$ is known. Therefore, some approximations for the exchange-correlation functional are developed since the exchange-correlation functional can not been known in Kohn-Sham equation.

Local spin density approximation (LSDA): Assume the exchange-correlation can be expressed in term of exchange-correlation density ϵ_{xc} which depends on electron density $n(\boldsymbol{r})$ and the magnitude $\boldsymbol{m}(\boldsymbol{r})$ of the spin density of homogeneous electronic gas as follows:

$$E_{xc}^{\mathrm{LSDA}}[n(\boldsymbol{r}), \boldsymbol{m}(\boldsymbol{r})] = \int n(\boldsymbol{r})\epsilon_{xc}(n(\boldsymbol{r}), m(\boldsymbol{r}))d\boldsymbol{r}. \tag{2.22}$$

The exchange field is aligned with the magnetization direction $\hat{\boldsymbol{m}}$ and can be expressed as follows:

$$\boldsymbol{B}_{xc}(\boldsymbol{r}) = n(\boldsymbol{r})\frac{\partial\epsilon_{xc}(n(\boldsymbol{r}), m(\boldsymbol{r}))}{\partial m(\boldsymbol{r})}\hat{\boldsymbol{m}}. \tag{2.23}$$

Structural properties of solid are often good, with a small different with experiments in calculating bulk lattice constants. The 'local' here means that only density in given point is known.

The generalized gradient approximation (GGA): The 'local'-density approximation above in some real atoms, molecule, or solids systems is less accurate because there is only density in given point is known. It is necessary to develop to another non-local approximation. A step toward the non-local generalization of this method is called the generalized gradient approximation (GGA) and expressed as:

$$E_{xc}^{GGA}[n_\uparrow, n_\downarrow] = \int f(n_\uparrow, n_\downarrow, \bigtriangledown n_\uparrow, \bigtriangledown n_\downarrow)d\boldsymbol{r}. \tag{2.24}$$

There are serval versions of the GGA method based on how to choose $f(n_\uparrow, n_\downarrow, \bigtriangledown n_\uparrow, \bigtriangledown n_\downarrow)$. Therein, the method established by Perdev, Burke, and Ernzerhof (PBE) [67] is used widely by its accuracy for magnetic systems than LSDA.

Basis sets for wave functions

There are several methods to create basis sets for atomic cores in all-electron Kohn-Sham wave functions $\psi_n(\vec{r})$ such as plane waves (PW) and the Augmented Plane Wave (APW)-based methods. The basis sets aim to get solutions with high accuracy and not so time-consuming.

Remind about Bloch theorem, it said that for a periodicity system like a crystal system, any eigenfunction can be expanded as [15]:

$$\psi_{\boldsymbol{k}}^{n}(\boldsymbol{r}) = \sum_{\boldsymbol{K}} u_{n\boldsymbol{k}} e^{i(\boldsymbol{k}+\boldsymbol{K})\cdot\boldsymbol{r}}. \tag{2.25}$$

This expansion contains the most simple choice for a basis set named PW basis set. Accompaniment with it, the PW basis set was fail to deal for the real crystal. Because potential near nuclei is very strong and the wavefunctions can not describe by PW functions.

The APW method was proposed originally by Slater [68] to deal with some cases that need information in the region near the nucleus. The APW basis set include atomic-like functions inside spheres called a 'muffin tin sphere' and plane waves in the remaining space outside the spheres called 'interstitial region':

$$\phi_{\boldsymbol{K}}^{\boldsymbol{k}} = \begin{cases} \frac{1}{\sqrt{V}} e^{i(\boldsymbol{k}+\boldsymbol{K})\cdot\boldsymbol{r}} & \text{in interstitial} \\ \sum_{lm} a_{lm\boldsymbol{k}}^{\mu\boldsymbol{K}} u_l^{\mu}(r_\mu, E_l^{\mu}) Y_{lm}(\hat{\boldsymbol{r}}_\mu) & \text{in muffin tin} \quad \mu \end{cases} \tag{2.26}$$

where $\boldsymbol{r}_\mu = r_\mu \hat{\boldsymbol{r}}_\mu = \boldsymbol{r} - \boldsymbol{r}_{o\mu}$ is the position in the system reference of the ionic position $\boldsymbol{r}_{o\mu}$. The Y_{lm} are spherical harmonics. The coefficient $a_{lm\boldsymbol{k}}^{\mu\boldsymbol{K}}$ are determined in order to the wave functions at the muffin tin continuous. Inside the muffin tin, the u_l^{μ} are solutions of the radial Schödinger equation for free atom at a given energy E_l^{μ}. In principle, the eigenvalue can be solved numerically. However, fixing E_l^{μ} leading a requirement of large number of APW basis functions and a limitation of number of energies for which a solution u_l^{μ} can be found.

One method was proposed by Andersen, Koelling, and Arbman [69,70] giving a better solution for the above problems. In this method, the wave functions inside spheres are expressed in a linear combination of different energy between

unknown-eigenenergy and a fixed energy as expressed in Eq. 2.27, it is so-called 'linearized augmented plane wave' (LAPW) basic sets.

$$u_l^\mu(r_\mu, \epsilon) = u_l^\mu(r_\mu, E_l^\mu) + (\epsilon - E_l^\mu)\frac{\partial u_l^\mu(r_\mu, E_l^\mu)}{\partial \epsilon}|_{\epsilon=E_l^\mu} + O(\epsilon - E_l^\mu)^2. \tag{2.27}$$

With this expansion, the LAPW method works well for a broad energy range of the valence bands. It was used with "full potential" in many modern studies [71].

Numerical procedures

It was well known that wave functions of core electron vary strong near the nuclei due to the strong Coulomb interaction and reduce when going far the nuclei. It is necessary to limit the basic set to perform calculation by introduce the radius $K_{\max}$, then it should be taken into account $K \leqslant K_{\max}$. The kinetic energy corresponding to $K_{\max}$ is called the cut off energy:

$$E_{\text{cut}} = \frac{\hbar^2 K_{\max}}{2m_e}. \tag{2.28}$$

A large cutoff energy is needed because core wavefunctions have sharply peaks near nuclei and the valence wavefunctions have lots of wiggles. The number of the plane wave is required being too large in most of cases. It leads to computational problems. Therefore, the pseudopotential methods were proposed to make tails of wavefunctions inside the atoms smooth. Then number of needed plane waves needed is only few.

Even the ultrasoft pseudopotential method achieved successfully in dealing with matters of localized elements, the problem is about the construction of these pseudopotential needing many parameter and requiring a lot of tests. Therefore, it was developed further to treat with that matter, the most successful approach and used widely nowadays named the projector augmented wave (PAW) method [72–74]. This is an extension of augmented wave methods and pseudopotential approaches [74].

In practice, the PAW and ultrasoft pseudopotentials often require larger cutoff energy for the charge density than for its plane wave because of their smoother

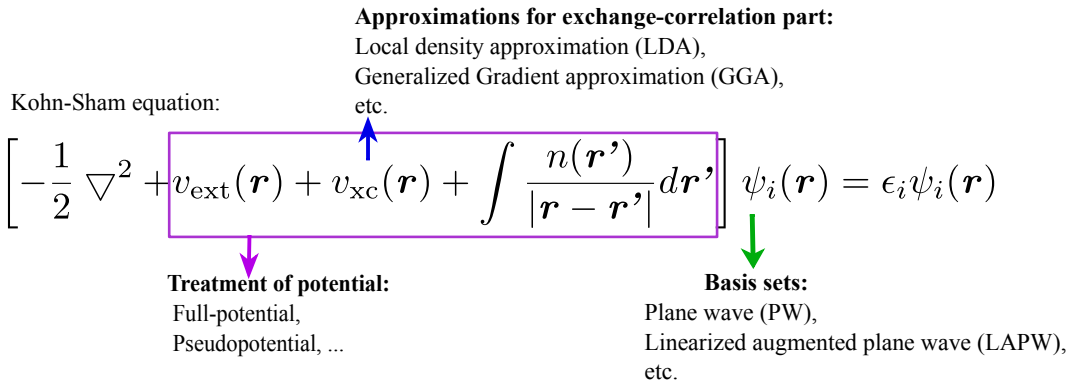

Figure 2.2: Variations in density-functional-theory calculations

leading an additional contribution of charge density compare with the square of the wave function. It was suggested that the cutoff energy for the charge density should be about 6-12 times larger for ultrasoft and PAW pseudopotential, and about 4 for norm-conserving pseudopotentials. However, in practice, it is necessary to test the convergence of this value.

2.2 Wannier functions

This section presents a representation named Wannier functions (WFs) which is an alternative representation for Bloch functions. This is an effective method to determine the electronic structure at any point in the phase space as well as to construct tight-binding models that are useful for evaluating materials properties, including the AH conductivity. The section firstly reviews basic definitions of Wannier function. It then presents a Wannier interpolation method applying for band structure and band derivative. Finally, the way how to obtain Berry curvature and anomalous Hall conductivity from Wannier interpolation is mentioned.

2.2.1 Basic definitions and properties

The electronic ground state of a periodic system is commonly described in a set of extended Bloch states $\psi_{n\boldsymbol{k}}(\boldsymbol{r})$ where the label $\boldsymbol{k}$ indicates a crystal momentum inside the Brillouin zone (BZ) and n is a band index. This representation is the most widely used in electronic structure calculations. However, Bloch states meet troubles to describe matters of local physical processes and phenomena originate from local electron correlations or impurities in materials.

In 1937, Gregory Wannier [75] proposed an alternative representation that can resolve these above matters named Wannier representation. The Wannier function (WF) of the nth isolated energy band at a cell $\boldsymbol{R}$ is a discrete Fourier transformation of the Bloch state:

$$|\boldsymbol{R}n\rangle = \frac{V}{(2\pi)^3}\int_{BZ} d\boldsymbol{k} e^{i\boldsymbol{k}\cdot\boldsymbol{R}} |\psi_{n\boldsymbol{k}}\rangle\,, \tag{2.29}$$

where V is the real-space primitive cell volume, the integral is carried over BZ and the WFs at different $\mathbf{R}$ in a crystal are translational images of one another. Then Bloch states $|\psi_{n\mathbf{k}}\rangle$ can be obtained by an inverse Fourier transform:

$$|\psi_{n\boldsymbol{k}}\rangle = \sum_{\boldsymbol{R}} e^{i\boldsymbol{k}\cdot\boldsymbol{R}} |\boldsymbol{R}n\rangle\,. \tag{2.30}$$

Wannier functions have been widely used in many applications and efficient for calculating material properties such as intrinsic AH conductivity and orbital magnetization.

2.2.2 Wannier interpolation

Interpolation of band structure

Wannier interpolation procedure starts from calculating first principles calculation on a coarse uniform reciprocal space $\boldsymbol{k}$ mesh. Therein the Hamiltonian matrix is noted as $H(\boldsymbol{k})$. Wannier functions, that localized in real space at position $\boldsymbol{R}$, are then constructed from Bloch states in selected bands j as in Eq. (2.29).

Eigenvalues at an arbitrary point $\boldsymbol{k}$ can be next interpolated by an inverse Fourier transformation:

$$\left|\psi^{\mathrm{W}}_{n\boldsymbol{k}}\right\rangle = \sum_{\boldsymbol{R}} e^{i\boldsymbol{k}\cdot\boldsymbol{R}} \left|\boldsymbol{R}n\right\rangle \qquad (n = 1, ..., j). \tag{2.31}$$

The Wannier interpolation procedure is summarized in Fig. 2.3.

The interpolated single-particle Hamiltonian reads:

$$H^{\mathrm{W}}_{nm}(\boldsymbol{k}) = \left\langle \psi^{\mathrm{W}}_{\boldsymbol{k}n}\middle|H\middle|\psi^{\mathrm{W}}_{\boldsymbol{k}m}\right\rangle = \sum_{\boldsymbol{R}} e^{i\boldsymbol{k}\cdot\boldsymbol{R}} \langle \boldsymbol{0}n|H|\boldsymbol{R}m\rangle. \tag{2.32}$$

where the notation $\langle \boldsymbol{0}n|$ indicates the nth Wannier function in the home unit cell $\boldsymbol{R} = 0$ (in Eq. 2.29). The superscript notes W that they are not eigenstates of Hamiltonian but belongs to "Wannier gauge". The eigenenergies are obtained by diagonalization 2.32 by unitary matrices $U(\boldsymbol{k})$ as follows:

$$H^{\mathrm{H}}_{nm}(\boldsymbol{k}) = [U(\boldsymbol{k})^{\dagger} H^{\mathrm{W}}(\boldsymbol{k}) U(\boldsymbol{k})]_{nm} = \delta_{nm} \bar{\epsilon}_n(\boldsymbol{k}). \tag{2.33}$$

Note that the Hamiltonian can be referred to as a tight-binding hopping Hamiltonian between localized orbitals:

$$H = \sum_{\boldsymbol{R}\boldsymbol{R}'} \sum_{nn'} H_{nn'}(\boldsymbol{R} - \boldsymbol{R}') |\boldsymbol{R}n\rangle\langle \boldsymbol{R}'n'|, \tag{2.34}$$

The interpolated band is plotted together with DFT bands to determine the accuracy of the interpolation procedure. In addition, it will be presented here another important content of the Wannier interpolation so-called interpolation of the derivative band energy [76]. It is useful to evaluate characteristics of materials.

Derivative of Hamiltonian in Wannier gauge

For quantities in transport coefficients, the derivative of the energy eigenvalues with respect to $\boldsymbol{k}$ has to take into account. For example, the anomalous Hall effect has been known to evaluate from Berry curvature which is related to Berry phase or geometric phase when a system is in adiabatic processes. In numerical

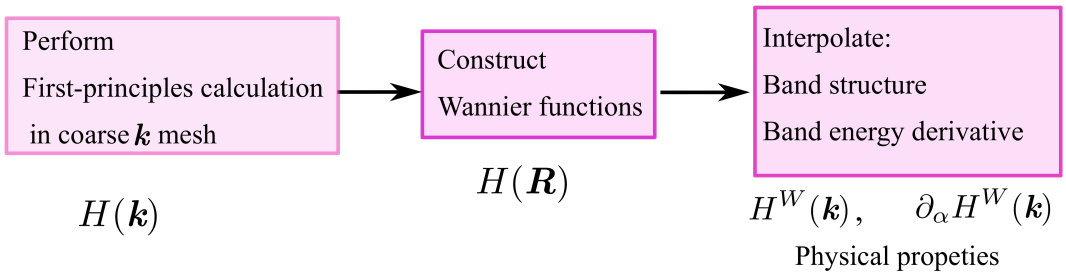

Figure 2.3: Wannier interpolation procedure.

calculation, the Brillouin zone integration can be replaced by a discrete summation of finite values on the $\boldsymbol{k}$-point mesh. It becomes a computational problem if the quantity under integration changes sharply in some regions. The quick variability of Berry curvature near band crossings makes a challenge to reach convergence. The derivative of Hamiltonian in Wannier gauge with respect to $\boldsymbol{k}$ can be written as:

$$H_\alpha^{\mathrm{W}}(\boldsymbol{k}) \equiv \partial_\alpha H^{\mathrm{W}}(\boldsymbol{k}) = \sum_{\boldsymbol{R}} e^{i\boldsymbol{k}\cdot\boldsymbol{R}} i R_\alpha \langle \boldsymbol{0}|H|\boldsymbol{R}\rangle, \tag{2.35}$$

where $\partial_\alpha = \partial/\partial k_\alpha$, and $\alpha = x, y, z$. In similar way, in general the above matrix is a non-diagonal matrix and needs to diagonalize by the rotated matrix $U(\boldsymbol{k})$. The actual band derivatives are:

$$\partial_\alpha \bar{\epsilon}_n(\boldsymbol{k}) = [U(\boldsymbol{k})^\dagger H_\alpha^{\mathrm{W}}(\boldsymbol{k}) U(\boldsymbol{k})]_{nn} \tag{2.36}$$

Berry curvature and anomalous Hall conductivity

As mentioned in Chap. 1, the AH conductivity is evaluated from the integral of Berry curvature over BZ:

$$\sigma_{\alpha\beta} = -\frac{e^2}{\hbar} \int \frac{d\boldsymbol{k}}{(2\pi)^3} \Omega_{\alpha\beta}(\boldsymbol{k}), \tag{2.37}$$

where total Berry curvature is the band summation:

$$\Omega_{\alpha\beta}(\boldsymbol{k}) = \sum_n f_n(\boldsymbol{k}) \Omega_{n,\alpha\beta}(\boldsymbol{k}). \tag{2.38}$$

Therein, the Berry curvature of band n is evaluated following the Kubo formula [22,77]:

$$\Omega_{n,\alpha\beta}(\boldsymbol{k}) = -2\mathrm{Im}\sum_{m\neq n}\frac{v_{nm,\alpha}(\boldsymbol{k})v_{mn,\beta}(\boldsymbol{k})}{[\epsilon_m(\boldsymbol{k})-\epsilon_n(\boldsymbol{k})]^2} \tag{2.39}$$

where the velocity operator is defined in term of the periodic part $u_{n\boldsymbol{k}}$ of the Bloch states:

$$v_{nm,\alpha}(\boldsymbol{k}) = \frac{1}{\hbar}\left\langle u_n(\boldsymbol{k})\left|\frac{\partial\hat{H}(\boldsymbol{k})}{\partial k_\alpha}\right|u_m(\boldsymbol{k})\right\rangle \tag{2.40}$$

with $\hat{H}(\boldsymbol{k}) = e^{-i\boldsymbol{k}.\boldsymbol{r}}\hat{H}e^{i\boldsymbol{k}.\boldsymbol{r}}$.

The quick variability of Berry curvature near band crossings can lead to a computational problem. Wannier interpolation supports a scheme to converge the AH conductivity calculation from integral of Berry curvature without using ultra-dense $\boldsymbol{k}$ mesh in BZ. Moreover, one powerful strategy was introduced by Wang, Yate, Souza, and Vanderbilt by $\boldsymbol{k}\cdot\boldsymbol{p}$ perturbation theory [22] to avoid the summation over all empty states as in Kubo formula. The idea in Ref. [78] start from the low-energy physics does not be affected in the large energy range above the Fermi level.

For transport properties like the AH effect, it only needs to construct WFs in a limited energy range called "inner window". The inner window energy range is often chosen from lowest energy band to a few eV above Fermi energy. Assume that there are M Wannier function per unit cell, then the total Berry curvature in Eq. 2.38 can expressed after Wannier interpolation as:

$$\Omega_{\alpha\beta}(\boldsymbol{k}) = \sum_{n=1}^{M} f_n(\boldsymbol{k})\Omega^{(\mathrm{H})}_{n,\alpha\beta}(\boldsymbol{k}). \tag{2.41}$$

Using definitions in Ref. [22] for the mth M-component vector matrix U being $||\phi_m\rangle\rangle$ and the perturbation theory with respect to $\boldsymbol{k}$ being:

$$||\partial_\alpha\phi_n\rangle\rangle = \sum_{l\neq n}\frac{\langle\langle\phi_l||\,\partial_\alpha H^{(W)}\,||\phi_n\rangle\rangle}{\epsilon_n^{(H)}-\epsilon_l^{(H)}}.\,||\phi_l\rangle\rangle \tag{2.42}$$

Define

$$D^{(\mathrm{H})}_{nm,\alpha} \equiv (U^\dagger \partial_\alpha U)_{nm} = \begin{cases} \frac{\bar{H}^{(\mathrm{H})}_{nm,\alpha}}{\epsilon^{(\mathrm{H})}_m - \epsilon^{(\mathrm{H})}_n} & \text{if} \quad n \neq m \\ 0 & \text{if} \quad n = m \end{cases} \tag{2.43}$$

where $\bar{O}^{(\mathrm{H})} = U^\dagger O^{(\mathrm{H})} U$ for an arbitrary matrix object O. Remember that Berry connection is not gauge-covariant and it can be written as:

$$A^{(\mathrm{H})}_\alpha = U^\dagger A^{(\mathrm{W})}_\alpha U + i U^\dagger \partial_\alpha U = \bar{A}^{(\mathrm{H})}_\alpha + i D^{(\mathrm{H})}_\alpha \tag{2.44}$$

The sum over occupied bands in terms of D and A matrixes:

$$\begin{aligned} \Omega_{\alpha\beta}(\boldsymbol{k}) = & \sum_{n=1} f_n(\boldsymbol{k}) \bar{\Omega}^{(\mathrm{H})}_{nn,\alpha\beta}(\boldsymbol{k}) + \sum_{nm} (f_m - f_n)(D^{(\mathrm{H})}_{nm,\alpha} \bar{A}^{(\mathrm{H})}_{nm,\beta} \\ & - D^{(\mathrm{H})}_{nm,\beta} \bar{A}^{(\mathrm{H})}_{nm,\alpha} + i D^{(\mathrm{H})}_{nm,\alpha} \bar{D}^{(\mathrm{H})}_{nm,\beta}). \end{aligned} \tag{2.45}$$

After evaluating D and A matrixes from Wannier interpolation including $\boldsymbol{k}$ derivatives, the total Berry curvature can be calculated straightforward. It was also demonstrated in Ref. [22] that the last term in 2.45 dominantly contributes to the total Berry curvature. This term has a Kubo-like form:

$$\Omega^{DD}_{\alpha\beta}(\boldsymbol{k}) = i \sum_{nm} (f_m - f_n) \frac{\bar{H}^{(\mathrm{H})}_{nm,\alpha} \bar{H}^{(\mathrm{H})}_{mn,\beta}}{[\epsilon^{(\mathrm{H})}_m - \epsilon^{(\mathrm{H})}_n]^2} \tag{2.46}$$

Using notion as in Eq. 2.42, it is also given as:

$$\Omega^{DD}_{\alpha\beta} = -2\mathrm{Im} \sum_{n=1}^{M} f_n \langle\langle \partial_\alpha \phi_n(\boldsymbol{k}) || \partial_\beta, \phi_n(\boldsymbol{k}) \rangle\rangle \tag{2.47}$$

here n indicate occupied bands.

Chapter 3

Results and discussion

In this chapter, the appearance of the AH effect is discussed along with symmetry operators including space-inversion and time-reversal symmetry according to symmetry of Berry curvature in the $\boldsymbol{k}$ space. Then the magnetic symmetry of Mn_3AN structure is analyzed by generating and classifying them following the multipole expansion scheme [30]. Magnetic structures that can induce finite AH effect in these compounds are also pointed out. The first-principle calculation results are then presented for stability of magnetic orderings which were generated and classified. Finally, it is intended to investigate the topological features of the AH effect in non-collinear AFM Mn_3AN.

3.1 Analysis of symmetry and anomalous Hall effect in Mn_3AN

Manganese nitrides Mn_3AN have the anti-perovskite crystal structure which belongs to the space group $Pm\bar{3}m$ (O_h^1, No. 221). The cubic unit cell of the structure have Mn atoms located at the face center, N atom at center and non-magnetic atom A at conner as introduced in Chap. 1. The symmetry-adapted multipole magnetic structure bases for Mn_3AN in Fig. 3.1 are generated following Ref. [30]

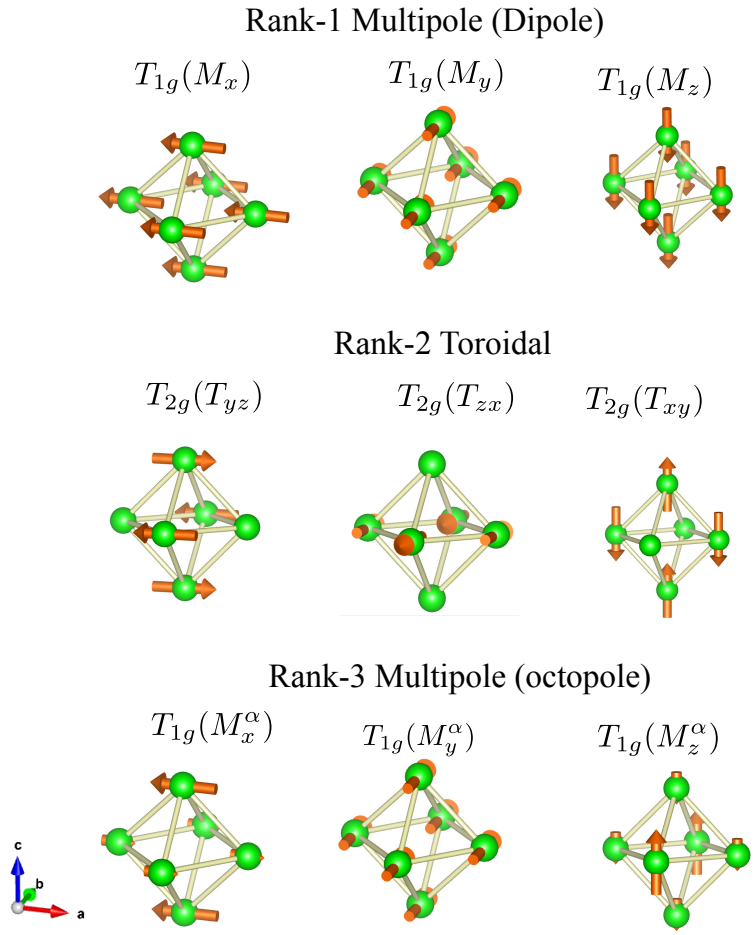

Figure 3.1: Magnetic configurations of Mn_3AN corresponding to the basis vectors.

and the method is also summarized in Appendix B in this thesis.

The energetically inequivalent magnetic structures with the ordering vector $\boldsymbol{q} = 0$ are classified and shown in Fig. 3.2. Therein, the magnetic (M)-dipole structures $(M_x, M_y, M_z) = (001)$, (110), and (111) represent ferromagnetic structures oriented along [001], [110], and [111] directions, respectively. The antiferromagnetic structures are obtained as the magnetic structures orthogonalized to the M-dipole structures [30] and are, in this compound, obtained as the rank-2 magnetic toroidal multipoles (MT-quadrupoles) and rank-3 M-multipoles (M-octupoles).

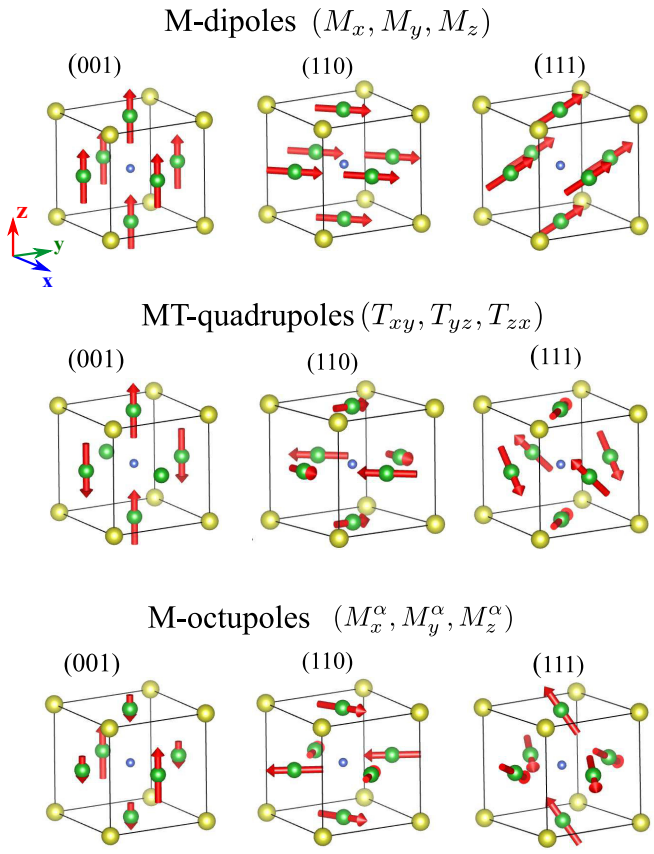

Figure 3.2: Energetically inequivalent magnetic structures of Mn_3AN classified according to the multipole moments following Ref. [12] and Ref. [30]. The green, yellow, and blue balls indicate Mn, A, and N atoms, respectively. Arrows on Mn atoms indicate the magnetic moments.

Table 3.1: Symmetry operations of magnetic point groups. The notations x, y and z are the Cartesian coordinates. E is the identity operator, $C_{n\mu}$, and m_ν indicate the n-fold rotation operator along μ axis and mirror plane corresponding with ν plane, respectively. I is the spatial inversion operator and T is the time-reversal operator.

No.	$4/mm'm'$	$4'/mm'm$	$\bar{3}m'$	$\bar{3}m$	$m'm'm$
1	E	E	E	E	E
2	C_{2z}	C_{2z}	$C_{3[111]}$	$C_{3[111]}$	C_{2z}
3	C_{4z+}	$C_{2[110]+}$	$C_{3[111]-}$	$C_{3[111]-}$	I
4	C_{4z-}	$C_{2[110]-}$	I	I	m_z
5	I	I	$IC_{3[111]}$	$IC_{3[111]}$	TC_{2x}
6	m_z	m_z	$IC_{3[111]-}$	$IC_{3[111]-}$	TC_{2y}
7	IC_{4z+}	$m_{[110]+}$	$Tm_{[\bar{1}01]}$	$m_{[\bar{1}01]}$	Tm_x
8	IC_{4z-}	$m_{[110]-}$	$Tm_{[1\bar{1}0]}$	$m_{[1\bar{1}0]}$	Tm_y
9	TC_{2x}	TC_{2x}	$Tm_{[01\bar{1}]}$	$m_{[01\bar{1}]}$	-
10	TC_{2y}	TC_{2y}	$TC_{2[\bar{1}01]}$	$C_{2[\bar{1}01]}$	-
11	$TC_{2[110]-}$	$Tm_{[110]-}$	$TC_{2[1\bar{1}0]}$	$C_{2[1\bar{1}0]}$	-
12	$TC_{2[110]+}$	$Tm_{[110]+}$	$TC_{2[01\bar{1}]}$	$C_{2[01\bar{1}]}$	-
13	TIC_{2x}	TIC_{2x}	-	-	-
14	TIC_{2y}	TIC_{2y}	-	-	-
15	$TIC_{2[110]-}$	$TIm_{[110]+}$	-	-	-
16	$TIC_{2[110]+}$	$TIm_{[110]-}$	-	-	-

Table 3.2: Classification of the magnetic structure with the ordering vector $\boldsymbol{q}$=0 in Mn_3AN according to the symmetry-adapted multipole [30] as well as the irreducible representation (IR) and magnetic point group (Mag. PG) with its principal axis (P. axis). The AH conductivity tensors (AHC) that can be finite under the magnetic point groups are also listed, where $\sigma_{110} \equiv \frac{1}{\sqrt{2}}(\sigma_{yz} + \sigma_{zx})$ and $\sigma_{111} \equiv \frac{1}{\sqrt{3}}(\sigma_{yz} + \sigma_{zx} + \sigma_{xy})$.

O_h-IR	Multipole	Mag. PG	P. axis	AHC
T_{1g}	$(M_x, M_y, M_z) = (001)$	$4/mm'm'$	[100]	σ_{yz}
	$= (010)$	$4/mm'm'$	[010]	σ_{zx}
	$= (001)$	$4/mm'm'$	[001]	σ_{xy}
	$= (110)$	$m'm'm$	[110]	σ_{110}
	$= (111)$	$\bar{3}m'$	[111]	σ_{111}
T_{2g}	$(T_{yz}, T_{zx}, T_{xy}) = (100)$	$4'/mm'm$	[100]	None
	$= (010)$	$4'/mm'm$	[010]	None
	$= (001)$	$4'/mm'm$	[001]	None
	$= (110)$	$mm'm$	[110]	None
	$= (111)$	$\bar{3}m$	[111]	None
T_{1g}	$(M_x^\alpha, M_y^\alpha, M_y^\alpha) = (100)$	$4/mm'm'$	[100]	σ_{yz}
	$= (010)$	$4/mm'm'$	[010]	σ_{zx}
	$= (001)$	$4/mm'm'$	[001]	σ_{xy}
	$= (110)$	$m'm'm$	[110]	σ_{110}
	$= (111)$	$\bar{3}m'$	[111]	σ_{111}

Orthogonalized multipoles which belong to T_{1g} and T_{2g} irreducible representation (IR) are listed in Table 3.2 together with the non-zero AH conductivity tensors. As shown in Table 3.2, the M-octupoles can induce the AH effect since these ordered states break the magnetic symmetry same as those of the M-dipoles [12]. On the other hand, MT-quadrupoles, which belong to T_{2g} IR, do not induce the AH effect with the magnetic structures shown in Fig. 3.2 due to the presence of the magnetic symmetry which forbids the finite AH conductivity as we demonstrate in the last part of Sec. 3.3.1. Symmetry operations of magnetic point groups presented in Table 3.2 are listed in Table 3.1.

As discussed in Ref. [12], co-planar magnetic structures induce no AH effect in the absence of spin-orbit coupling (SOC) in general by the presence of the "effective time-reversal symmetry" R_sT, which is the symmetry of conjunct operation of time reversal T and global spin rotation R_s. Note that conventional unit cells of non-collinear magnetic structures $(T_{yz}, T_{zx}, T_{xy}) = (111)$ and $(M_x^\alpha, M_y^\alpha, M_y^\alpha) = (111)$ include only three Mn atoms making an atom plane and their magnetic moments all lying on that plane. Therefore, not only ferromagnetic ordering (*i.e.* M-dipoles) but also all listed above magnetic structures (*i.e.* M-octupoles) with the co-planar AFM spin configurations require SOC to induce the AH effect due to the R_sT symmetry preserved in the absence of SOC as the 180° spin rotation. In the following section, we proceed to the quantitative evaluation of the AH conductivity for the M-octopole structures based on the results of first-principles calculations considering SOC.

3.2 Stability of magnetic ordering in Mn_3AN

3.2.1 Computational details

The stability of magnetic structures in Mn_3AN is considered by comparing total energies calculated by the first-principles approach. QUANTUM ESPRESSO package [79] is used to perform the density functional theory calculations and

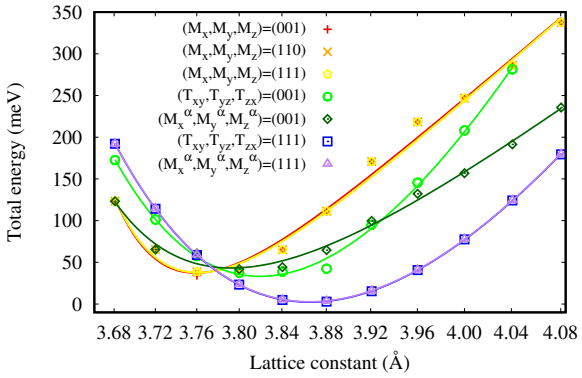

Figure 3.3: Total energy as a function of lattice constants for different magnetic configurations in Mn_3GaN. The equilibrium total energy of the $(M_x^\alpha, M_y^\alpha, M_z^\alpha) =$ (111) magnetic structure is chosen as the origin of total energy. The values are fitted to Birch-Murnaghan's equation of state [87] by the least square method.

to evaluate the electronic and magnetic properties of antiperovskite manganese nitrides. Generalized gradient approximation in the parametrization of Perdew, Burke, and Ernzerhof [67] is used for the exchange-correlation functional. The pseudopotentials in the projector augmented-wavemethod [80] are generated by PSLIBRARY [81]. We choose kinetic cut-off energies 100 Ry and 800 Ry for the plane wave basis set and charge density, respectively.

3.2.2 Magnetic stability of Mn_3AN

The optimization of lattice constants for each magnetic structure in Mn_3AN are performed by calculating lattice constant dependence of the total energy as shown for Mn_3GaN in Fig. 3.3. The optimized lattice constants agree with previous experimental values [82,83]. It is shown that either (T_{yz}, T_{zx}, T_{xy})= (111) or $(M_x^\alpha, M_y^\alpha, M_z^\alpha)$= (111) is obtained as the stable magnetic structure in Mn_3AN. The thesis hereafter focus on these (111) non-collinear AFM structures and refer the magnetic structures of (T_{yz}, T_{zx}, T_{xy})= (111) and of $(M_x^\alpha, M_y^\alpha, M_z^\alpha)$= (111) as MT-quadrupole (MTQ) and M-octupole (MO), respectively, following the multipole

Table 3.3: Equilibrium lattice constants a_0(Å), local magnetic moments $|m_{\text{local}}|(\mu_{\text{B}})$, and the difference of total energy ΔE (meV) between (111) magnetic orderings and the M-octupole (M_x^α, M_y^α M_z^α)= (111) (MO) configurations. The bold values indicate the lowest ΔE. The M-dipole (M_x, M_y, M_z)= (111) and M-T quadrupole (T_{yz}, T_{zx}, T_{xy})= (111) are referred as the FM [111] and the MTQ configuration, respectively.

This work						**Experiments**
A	Config.	a_0(Å)	$\lvert m_{\text{local}}\rvert$ (μ_B)	$\lvert m_{\text{total}}\rvert$ (μ_{B})	ΔE (meV)	Magnetic configurations (temperature)
Ni	FM [111]	3.827	3.12	9.35	345.5	• MO + MTQ ($10K < T < 250K$) [41]
	MTQ	3.832	2.99	0.0	0.04	• MO + MTQ ($160K < T < 266K$) [39]
	MO	3.832	2.99	0.0	**0**	
Cu	FM [111]	3.851	2.74	8.23	257.8	
	MTQ	3.853	2.87	0.0	**-7.5**	• Ferromagnetic in tetragonal
	MO	3.853	2.97	0.10	0	($T < 150K$) [84]
Zn	FM [111]	3.781	1.510	4.53	190.8	• AFM but not MTQ ($T < 80K$) [85]
	MTQ	3.866	2.74	0.0	**-0.4**	• MTQ ($80K < T < 170K$) [39, 85]
	MO	3.866	2.74	8.23	0	
Ga	FM [111]	3.757	1.07	3.23	124.8	
	MTQ	3.865	2.61	0.00	**-0.4**	• MTQ ($T < 298K$) [39]
	MO	3.865	2.61	0.08	0	
Ge	FM [111]	3.756	0.91	2.73	146.3	
	MTQ	3.858	2.49	0.0	**-8.6**	-
	MO	3.858	2.49	0.0	0	
Pd	FM [111]	3.949	3.21	9.66	474.6	
	MTQ	3.927	3.36	0.0	**-9.5**	-
	MO	3.927	3.34	-0.01	0	
In	FM [111]	3.910	1.56	4.68	329.3	• Weak FM+ AFM ($T < 175K$) [85]
	MTQ	3.989	2.61	0.0	74.6	• AFM ($175K < T < 300K$) [85]
	MO	3.989	2.91	0.05	**0**	
Sn	FM [111]	3.882	1.193	3.58	236.7	• Complex ($T < 237K$) [86]
	MTQ	3.851	2.01	0.0	215.6	• MO and MTQ
	MO	3.982	2.75	0.0	**0**	($237K < T < 357K$) [39, 86]
Ir	FM [111]	3.870	2.94	8.81	807.8	
	MTQ	3.863	2.77	0.00	**-3.0**	-
	MO	3.863	2.77	0.06	0.0	
Pt	FM [111]	3.949	3.25	9.66	483.0	
	MTQ	3.927	3.23	0.0	**-6.7**	-
	MO	3.927	3.23	- 0.05	0	

characterization of the magnetic structure proposed in Refs. [12] and [30]. The total energies for ferromagnetic, MTQ, and MO magnetic structures are listed with the relative energy from the MO magnetic structure, *i.e.* $\Delta E = E - E_{\mathrm{MO}}$, for the series of Mn_3AN.

The table shows that Mn_3AN with A = Ni, In, Sn prefer the MO configuration, and those with the other A atoms prefer the MTQ configuration, having the MO magnetic structure as the secondary stable solution. The energy differences between the MO and MTQ magnetic structures are small for most of the Mn_3AN compounds. Mn_3NiN shows only tiny energy difference of 0.04 meV/Mn, which explain the experimentally reported possible coexistence of the MO and MTO phases [41]. On the other hand, we may expect that Mn_3InN and Mn_3SnN are stabilized to the MO phase with $\Delta E(\mathrm{MTQ} - \mathrm{MO}) \sim 74.6$ meV and 215.6 meV and active for the AH effect. The presence of weak ferromagnetism in AFM states observed for Mn_3InN [85] implies that the observed AFM structure is the MO structure since the MO and ferromagnetic structures belong to the same magnetic symmetry and can coexist in the magnetic phase. In the followings, thesis will focus on the AH effect in the MO magnetic structure, which is the first or secondary stable solution for all of Mn_3AN and can induce the AH effect.

3.3 Anomalous Hall conductivity in non-collinear AFM Mn_3AN

This section shows an overall the relation between Berry curvature and electronic structure in series non-collinear AFM Mn_3AN. The AH conductivities are evaluated along with the Fermi energy dependencies. The change in AH conductivity is checked by tuning hopping integrals. The analysis of density of state for time-reversal pair of Mn-spin clusters for non-collinear AFM system, in particular, Mn_3AN is also mentioned. Band filling effect is discussed as the number of valence electrons is increased one by one for a group material.

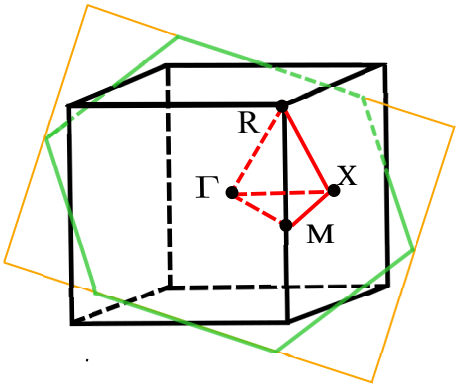

Figure 3.4: The first Brillouin zone (black) corresponding to the crystal primitive unit cell with the high symmetry points.The hexagonal plane (green line) shows minimum periodicity in the (111) plane for the simple cubic Brillouin zone with the center point at Γ. The orange rectangular is the region used to plot the Berry curvature in Figs. 3.5, 3.7, and 3.8.

3.3.1 Berry curvature in Mn_3AN

The first Brillouin zone (BZ) with minimum periodicity in the (111) plane for the simple cubic Brillouin zone with the center point at Γ is shown in Fig. 3.4. The presence of Berry curvature after taking band summation, $\Omega^{111}_{\rm sum}(\boldsymbol{k}) \equiv \frac{1}{\sqrt{3}}(\Omega_{yz,\rm sum}(\boldsymbol{k}) + \Omega_{zx,\rm sum}(\boldsymbol{k}) + \Omega_{xy,\rm sum}(\boldsymbol{k}))$ with $\Omega_{\alpha\beta,\rm sum}(\boldsymbol{k}) = \sum_n f[\epsilon_n(\boldsymbol{k}) - \mu]\Omega_{n,\alpha\beta}(\boldsymbol{k})$, in $\boldsymbol{k}$ space is visualized in Fig. 3.5 in Mn_3IrN for MO magnetic structure. It shows the highest peak at $\Gamma_{0.195}$ =(0.195, 0.195, 0.195). Let's see where the center of Berry curvature peak comes from. Electronic band structure and the corresponding Berry curvature in a $\boldsymbol{k}$ part across Γ point in case without SOC and with SOC are shown in Fig. 3.6. It shows that with the presence of SOC, band splitting near the Fermi creates two occupied and unoccupied bands in short range of energy leading to the finite Berry curvature as shown in Fig. 3.6 (d). How Berry curvature changes for a pair materials Mn_3GaN and Mn_3InN is shown in Fig. 3.7. Two elements Ga and In have the same number of valence electrons and therefore the electronic bands are quite similar as shown in 3.7 (a) and (b). However, the little bit different

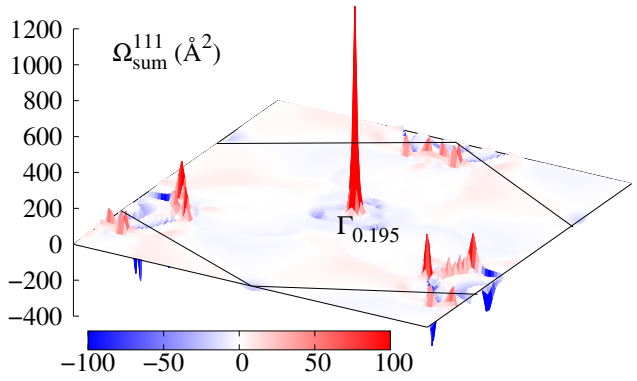

Figure 3.5: The Berry curvature after taking band summation on (111) plane centered at $\Gamma_{0.195}$ =(0.195, 0.195, 0.195) for MO magnetic structure in Mn_3IrN.

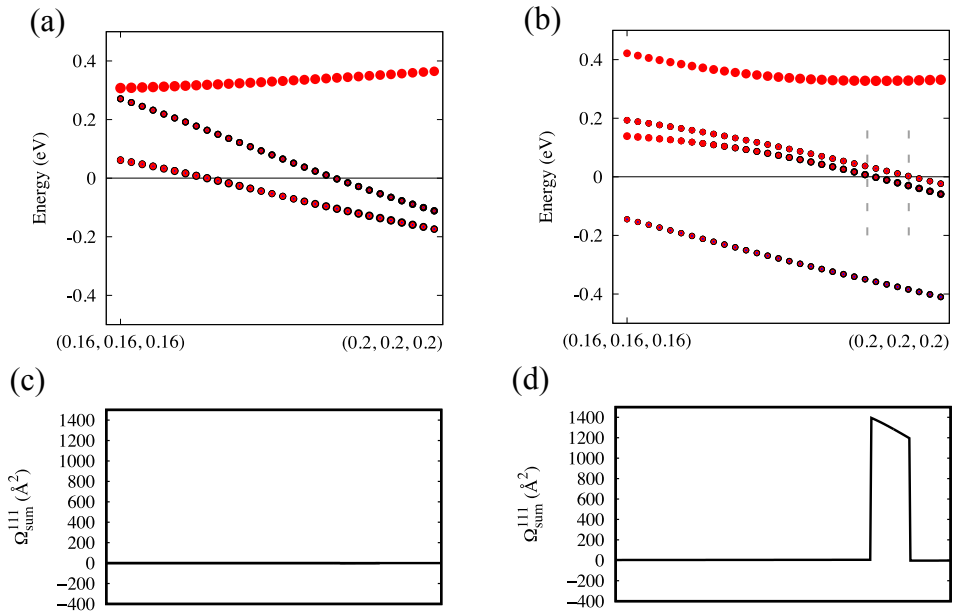

Figure 3.6: Electronic band structure in Mn_3IrN in case without SOC(a), with SOC (b) and the corresponding Berry curvature (c) and (d). The point $\Gamma_{0.195}$ in Fig. 3.5 is located in the region between two dashed lines shown in (b).

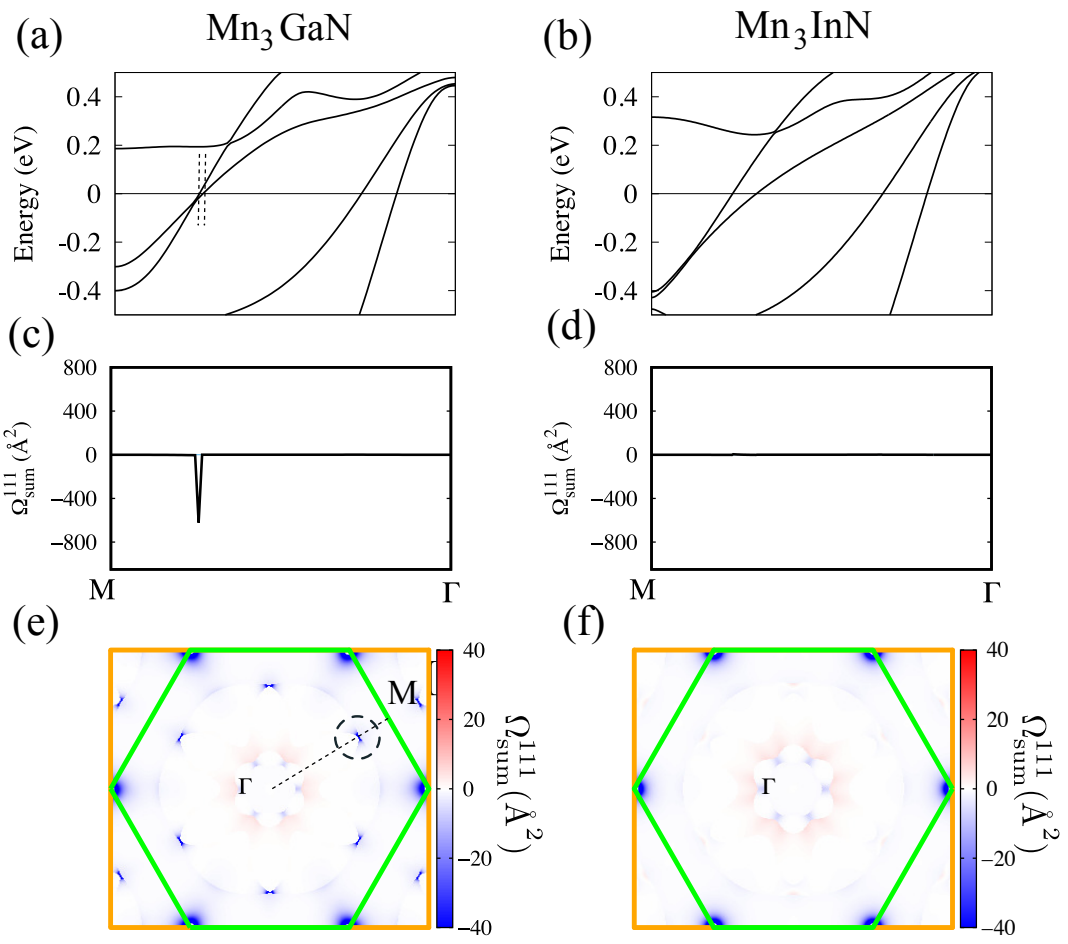

Figure 3.7: Electronic band structure along ΓM in (a) Mn_3GaN, (b) Mn_3InN for MO magnetic structure and the corresponding Berry curvature (c) and (d). The Berry curvature after taking band summation on (111) plane centered at Γ in (e) Mn_3GaN and (f) Mn_3InN.

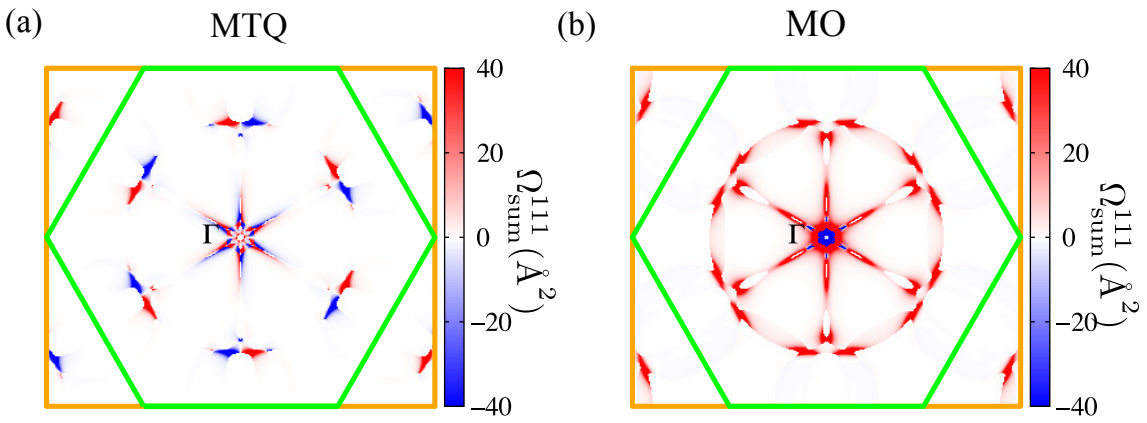

Figure 3.8: The [111] Berry curvature component after taking band summation, $\Omega^{111}_{\rm sum}(\text{Å}^2) \equiv \frac{1}{\sqrt{3}}(\Omega_{yz,\rm sum} + \Omega_{zx,\rm sum} + \Omega_{xy,\rm sum})$, on (111) plane centered at Γ, shown in Fig. 3.4, for Mn_3GeN (a) MTO and (b) MO configuration, respectively.

band structure near the Fermi level leads to a large change in the Berry curvature as shown in Fig. 3.7 (c), (d), (e), and (f). The absence of the Berry curvature region in $\boldsymbol{k}$ space in Mn_3InN may lead to the difference of the AH conductivity comparing with Mn_3GaN.

The difference in symmetry of the Berry curvature for the MO and MTQ magnetic structures is then illustrated to see how the Berry curvature cancels out after integral overall Brillouin zone for a given magnetic configuration. Figure 3.8 shows distribution of the Berry curvature component after taking band summation on the (111) plane shown in Fig. 3.4 for the MO and MTQ magnetic structures. The MO and MTQ magnetic structures belong to the magnetic point groups $\bar{3}m'$ and $\bar{3}m$, respectively, and the Berry curvature distribution keeps the three-fold rotation symmetry on the (111) plane. In contrast to the MO magnetic structure, the MTQ magnetic structure cancels out the Berry curvature on the (111) plane with BZ integration due to the mirror symmetry with the vertical mirror planes and leads to no AH conductivity for the magnetic structure.

3.3.2 Anomalous Hall conductivity

The Berry curvature and AH conductivity are evaluated by using the tight-binding models generated from the first-principles calculations [22] by Wannier interpolation scheme using Wannier90 [88]. Including s, p, d orbitals for Mn and A atoms and s, p orbitals for N atoms, the obtained tight-binding models show almost complete reproducibility of the energy bands for those obtained from the first-principles calculations within the energy interval from the lowest energy of the valence bands to about 4 eV above the Fermi energy for the Mn_3AN series, as shown in Fig. 3.9 for Mn_3GeN, Mn_3PdN and Mn_3IrN. A $\boldsymbol{k}$-mesh 18×18×18 is utilized to sample the first Brillouin zone (BZ) with Methfessel-Paxton smearing width of 0.005 Ry to get the Fermi level. The AH conductivity was evaluated with the uniform $\boldsymbol{k}$-point mesh of 200×200×200 with the adaptive $\boldsymbol{k}$-mesh refinement [89,90] of 5×5×5 for the absolute values of Berry curvature larger than 100Å^2.

The AH conductivity, $\sigma_{111} \equiv \frac{1}{\sqrt{3}}(\sigma_{yz} + \sigma_{zx} + \sigma_{xy})$ have been calculated for the magnetic structures shown in Fig. 3.2 and listed the values in Table 3.4. Note that the conductivity (σ_{yz}, σ_{zx}, σ_{zy}) has the transformation property for the magnetic point group same as that for the magnetization (M_x, M_y, M_z) [12], and the time-reversal counterparts of the magnetic structures hold the opposite sign to the AH conductivity. Some of Mn_3AN materials show large AH conductivity in the non-collinear AFM magnetic structure as the same order of the AH conductivity calculated for the ferromagnetic states such as Fe (750 S/cm) [22,89] and Co (480 S/cm) [91]. The AH conductivity values for the non-collinear antiferromagnet Mn_3Ir, which shows the same magnetic alignment on Mn atoms in Mn_3AN, is also evaluated in this work as 233.8 S/cm and in good agreement with the previous work (218 S/cm) [5].

Some of the AH conductivities theoretically predicted in these compounds are the same order in this work as listed in Table 3.4. The difference in its value may come from the details of first-principles calculations such as adopting of lattice constants from experiments or from optimization procedures. The AH

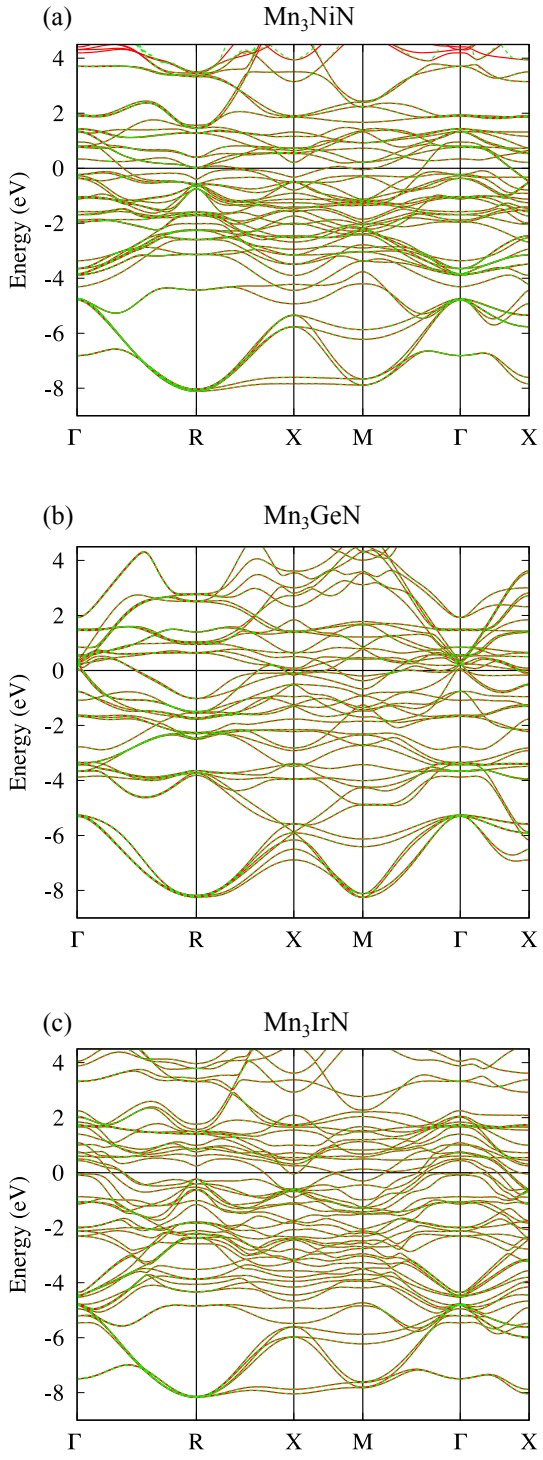

Figure 3.9: Energy bands from the first-principles calculations (red) and from Wannier interpolation (green) of (a) Mn_3NiN, (b) Mn_3GeN, and (c) Mn_3IrN along high symmetry points in the first Brillouin zone of a simple cubic shown in Fig. 3.4.

Table 3.4: Calculated AH conductivity, σ_{111}, for the MO magnetic configuration in Mn_3AN compounds.

	Mn_3AN	This work	References
σ_{111} (S/cm)	Mn_3NiN	375.7	-301 [42]* -294.5 (σ_{xy} =-170) [92]* 225.2 (σ_{xy} = 130) [93]**
	Mn_3CuN	-287.7	-
	Mn_3ZnN	350.5	-232 [42]*
	Mn_3GaN	96.3	-99 [42]* 69.3 (σ_{xy}=40) [93]**
	Mn_3GeN	-624.5	-
	Mn_3PdN	252.6	-
	Mn_3InN	34.6	-
	Mn_3SnN	-128.0	230.4 (σ_{xy} = 133) [93]**
	Mn_3IrN	-575.3	-
	Mn_3PtN	799.9	-

*Magnetic moments assumed to calculate the AH conductivity are opposite to those of this work.

**The sign of the AH conductivity listed in Ref. [93] is uncertain.

conductivity was recently reported for thin films of Mn_3NiN as $|\sigma_{xy}| = 15$ S/cm at 150K under no external magnetic field [92], which is one order smaller than the theoretical prediction. The large difference with the experiment and theoretical prediction can be addressed to the possible mixing of the MO and the MTQ magnetic structures as discussed in Ref. [92].

The Fermi energy dependence of the AH conductivity is depicted in Fig. 3.10. Each graph contains results of Mn_3AN with A elements in the same period (period 4: Cu, Zn) or the same group (group 10: Ni, Pd, Pt), (group 13: Ga, In), (group 14: Ge, Sn) in the periodic table and the result for Mn_3IrN is shown together with Mn_3Ir.

3.3.3 Tuning hopping integrals

In order to clarify the dependency of AH conductivity on size of Mn-spin moment, a tight-binding model which intermediate the nonmagnetic state and the MO magnetic state are employed. The Hamiltonian is written as $H_\lambda = H_{\rm nmag} + \lambda(H_{\rm mag} - H_{\rm nmag})(\lambda \geqslant 0)$ [12], where λ is an interpolating parameter that represents development of the MO magnetic ordering. The Hamiltonian matrix elements for magnetic state $H_{\rm mag}$ and one for nonmagnetic state $H_{\rm nmag}$ are taken from Wannier-basis hopping terms projected from the first-principles calculations.

As shown in Fig. 3.11, the AH conductivity first increases with negative sign with λ, then shows maximum value at $\lambda = 0.5$, and finally decreases and change the sign to positive (at $0.6 < \lambda < 1.2$). Here we compare the density of states (DOS) between MO magnetic state (λ=1) and intermediate magnetic state (λ=0.5). DOS is projected not onto the spin states (*i.e.* up- and down-spin states) but projected onto the time-reversal pair of Mn-spin clusters, characterized by $+M^{\alpha}_{(111)}$ and $-M^{\alpha}_{(111)}$, as shown in Fig. 3.11(a).

In Fig. 3.11(c), MO magnetic state shows DOS where the majority Mn-spin-cluster state is almost fully occupied as having the small weight at the Fermi energy, whereas minority Mn-spin-cluster state has large weight at the Fermi

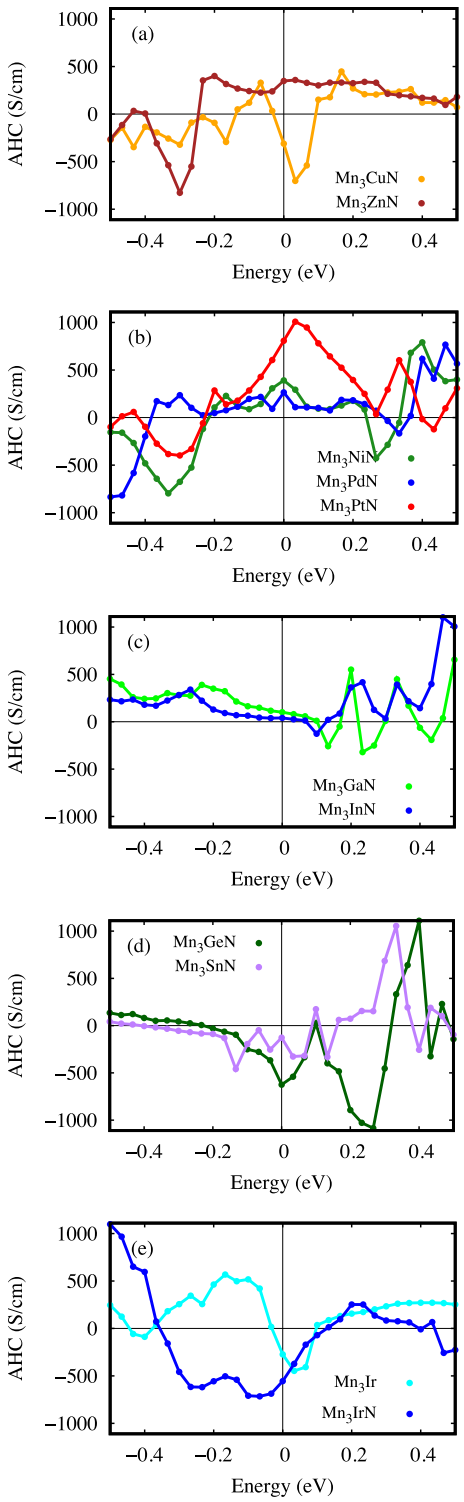

Figure 3.10: The Fermi energy dependence of AH conductivity for Mn_3AN compounds. The origin of the energy is the Fermi energy from the first-principles calculation.

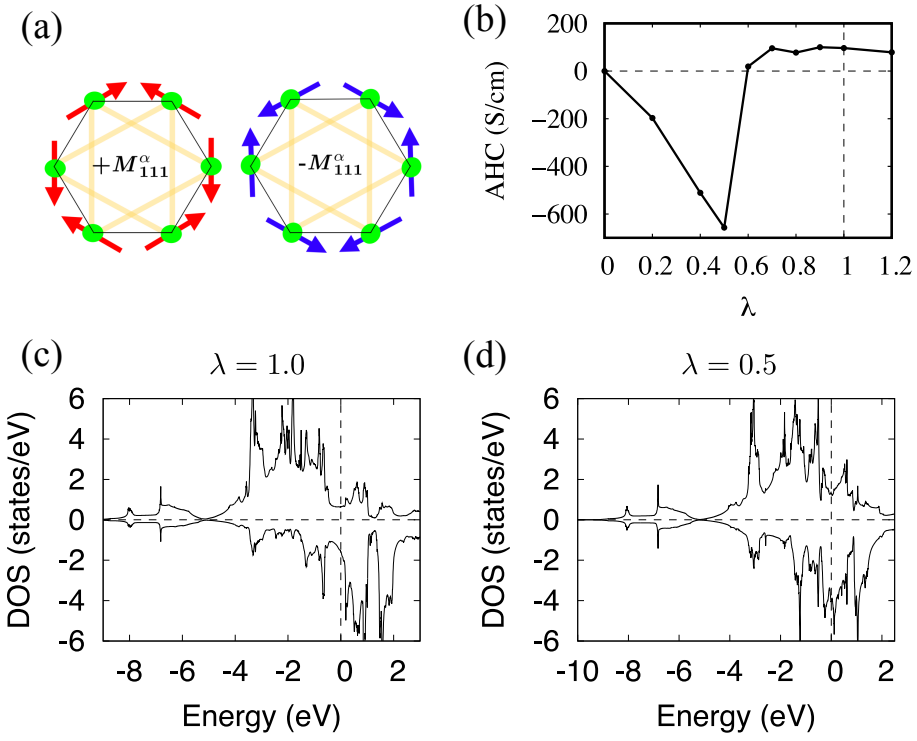

Figure 3.11: (a) Two Mn-spin cluster moments of the MO magnetic state for Mn_3AN. (b) The dependence of AH conductivity on the interpolating parameter (λ) in tight-binding model of Mn_3GaN. Density of states (DOS) and the corresponding AH conductivity value of Mn_3GaN with $\lambda = 1.0$ and $\lambda = 0.5$ are shown in diagram (c) and (d), respectively. The black line upper panel indicates the DOS of $+M^{\alpha}_{111}$ Mn-spin cluster moment, and the one in lower panel indicates the negative cluster moment $-M^{\alpha}_{111}$.

energy as contributing to the AH conductivity. As shown in Fig. 3.11(d), the intermediate magnetic state shows rather large DOS at the Fermi energy both in the Mn-spin-cluster states. The difference between the majority and minority Mn-spin-clusters may explain the enhancement of the AH conductivity at λ=0.5.

3.3.4 Band filling effect

The band filling effect in a group of Mn_3AN with A = Cu, Zn, Ga, and Ge elements belonging to period 4 in the periodic table is considered. Figure 3.13 shows band projection and corresponding Berry curvature along the $\boldsymbol{k}$ point path in Mn_3AN while the number of valence electrons is increased one by one from Mn_3CuN to Mn_3GeN.

DOS for Mn-spin clusters states for this group materials are shown in Fig. 3.12 However, the large Mn-spin cluster DOS do not guarantee large AH conductivity. It depends on detailed band structure around the Fermi energy. As the band structure shows large change in this group materials, the evaluation can be only fairly judged for them. As an example of comparing with Mn_3CuN, the presence of more negative Berry curvature as pointed by a dashed line in Fig. 3.13 (c) and (d) leading to more positive AH conductivity for Mn_3ZnN. There is a main contribution of Mn d-orbital band near the Fermi level in most compounds and the contribution from other orbitals are quite small except for Mn_3GeN. The Ge p-orbital (blue) in Mn_3GeN is partly occupied, then it can hybridize with Mn d-orbital (red-brown) and partly contribute to a larger AH conductivity in Mn_3GeN than with other compounds. The presence of Ga 4p-orbital and Ge 4p-orbital peaks are shown in Fig. 3.14.

Note that, the next section will show that the divergent Berry curvature does not dominantly contribute to the AH conductivity. The Berry curvature can have drastically large peaks by the mechanism explained here. Nevertheless, those spiky Berry curvature cannot be the main factor to enhance the AH conductivity.

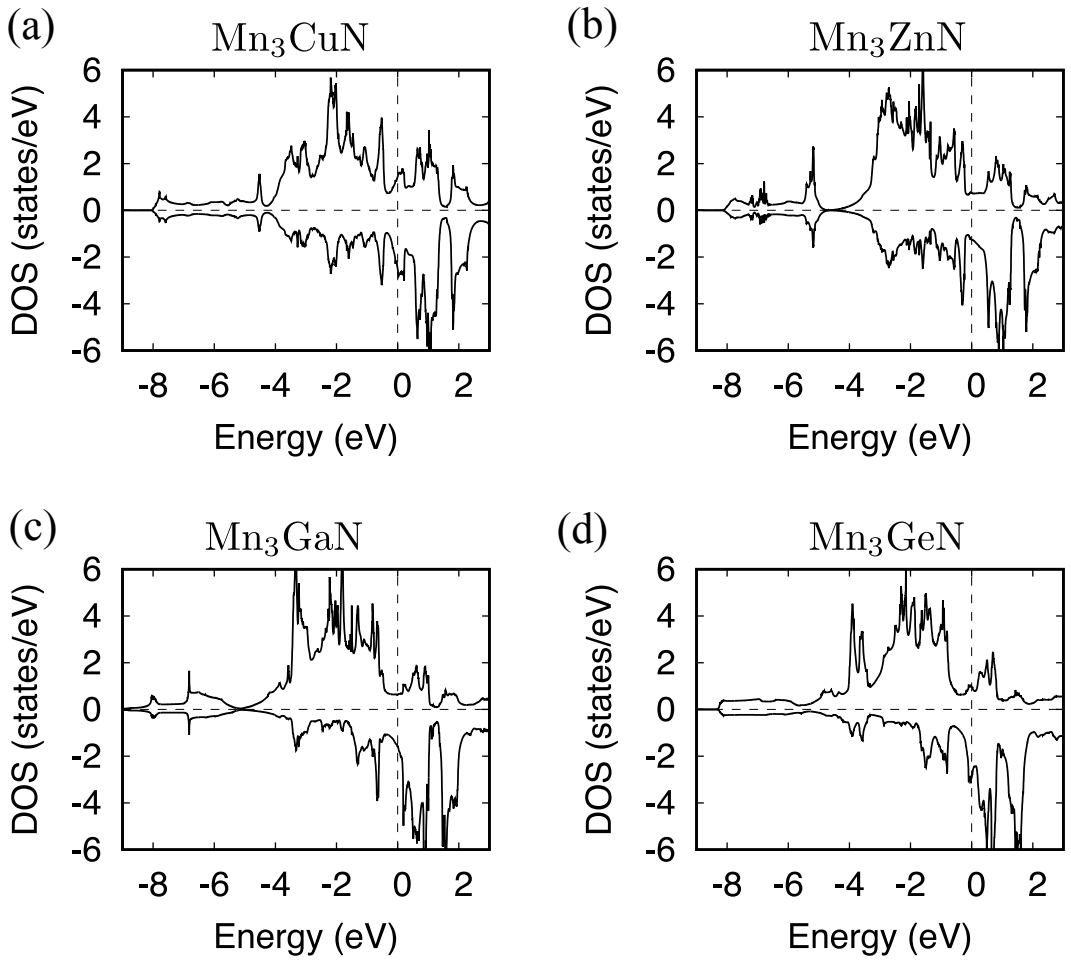

Figure 3.12: Density of state (DOS) of Mn-spin clusters in (a) Mn_3CuN, (b) Mn_3ZnN, (c) Mn_3GaN, and (d) Mn_3GeN.

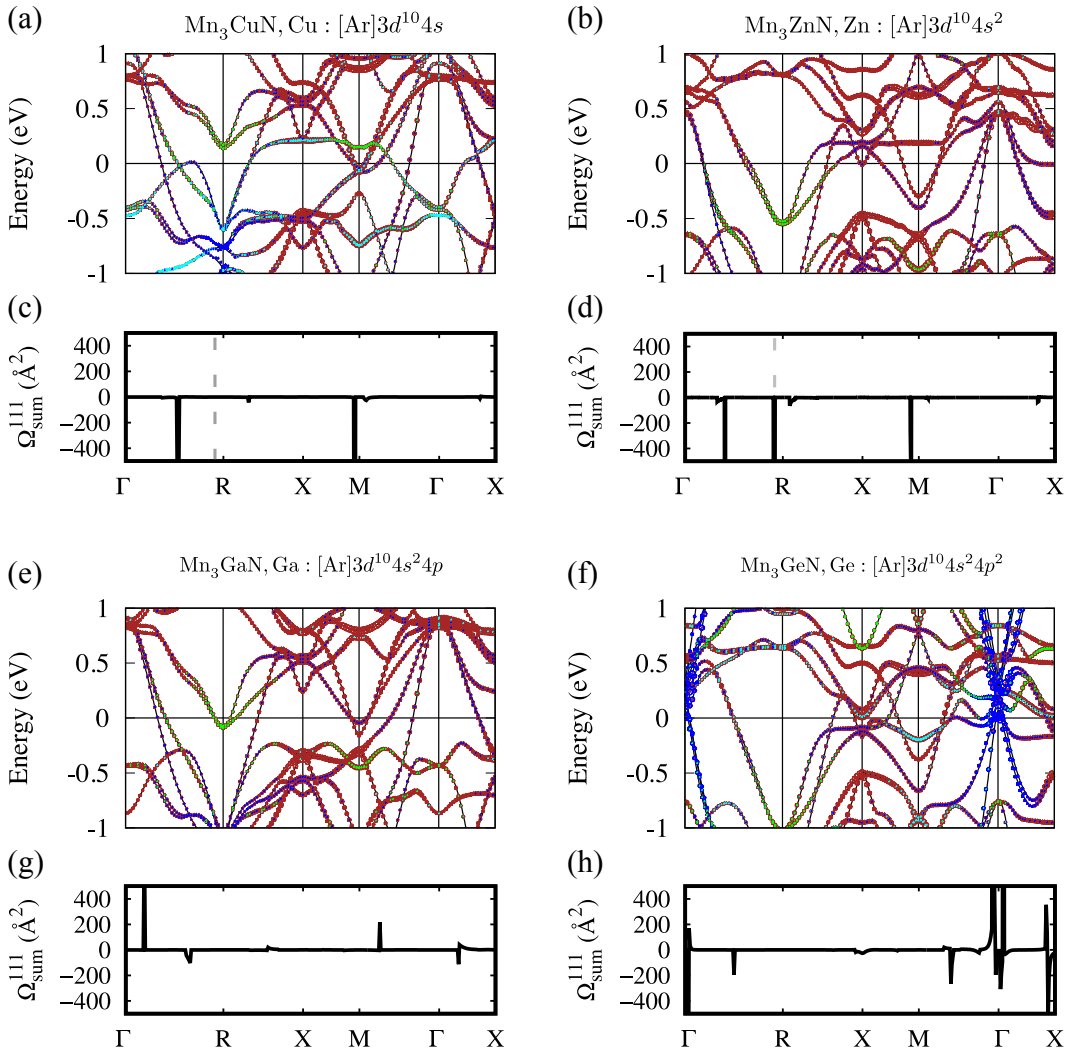

Figure 3.13: Band projection in (a) Mn_3CuN, (b) Mn_3ZnN, (e) Mn_3GaN, (f) Mn_3GeN and the corresponding Berry curvature along the $\boldsymbol{k}$ point path in (c) Mn_3CuN, (d) Mn_3ZnN, (g) Mn_3GaN, (h) Mn_3GeN. In the band projection panel, the black color band structure is for all components, and the red-brown color indicates Mn d-orbital projection. In the Berry curvature panel, cyan, blue, and green are for A d-orbital, A p-orbital and A s-orbital, respectively. The grey dashed lines indicate the position which Berry curvature is different between Mn_3CuN and Mn_3ZnN.

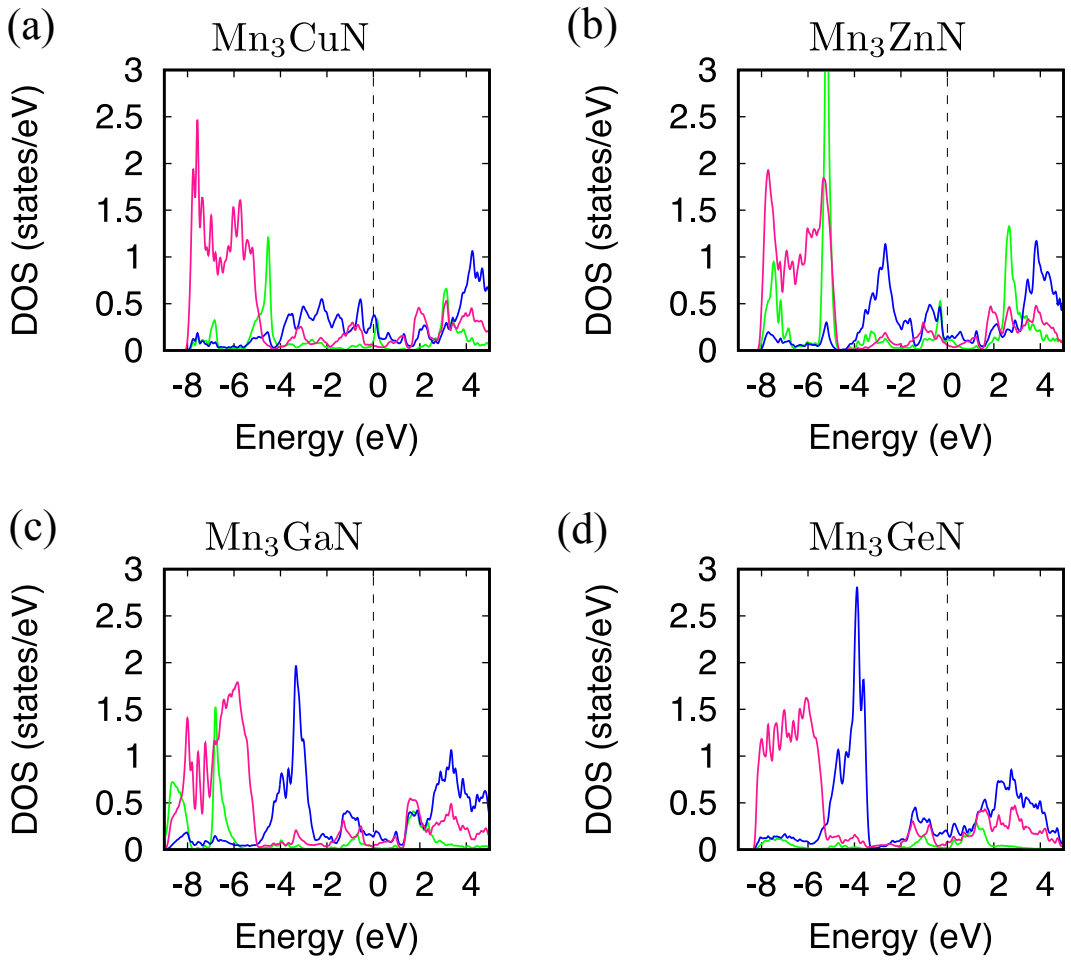

Figure 3.14: DOS of orbital project of A p-orbital (blue) and A s-orbital (green), and N p-orbital (pink) for a series compounds (a) Mn3CuN, (b) Mn3ZnN, (c) Mn3GaN, (d) Mn3GeN.

3.4 Topology analysis

This section is intends to investigate topological features of the AH effect in non-collinear AFM Mn_3AN.

3.4.1 Berry curvature and Weyl points

In Weyl semimetal, it has been often suggested that the Berry curvature around the Weyl points dominantly contribute to the AH effect in the local $\boldsymbol{k}$ space regions [43, 44]. For metallic magnets, Martínez *et al.* suggested that the Fermi sheets with Weyl points very nearby tend to contribute more to the AH conductivity than other Fermi sheets farther from Weyl points by investigating ferromagnetic bcc Fe [24]. In this section, we investigate the Berry curvature, Weyl points which characterize the topology aspects of the magnetic structures, and their roles in the resultant AH effect for the AFM states in Mn_3AN. Weyl points are determined by examining chirality for possible energy crossing points. The converged number of Weyl points in BZ is obtained by increasing $\boldsymbol{k}$-point mesh in the first BZ to search the crossing points, and the chirality is calculated from the Berry flux coming out of a small sphere S surrounding each Weyl point, *i.e.* $\frac{1}{2\pi}\oint_S dS\hat{\mathbf{n}}.\boldsymbol{\Omega}_n(\mathbf{k})$ [24].

A schematic picture of Berry curvature divergence around a Weyl point in Fig. 3.15 shows the Weyl point acts as a source of Berry flux in Fig. 3.15 (a) and the divergent behavior of Berry curvature along one direction as in Fig. 3.15 (b). When consider band summation, the Berry curvature can show finite values as in Fig. 3.15 (e) and (f). Two bands in the left hand side of Fig. 3.15 (d) are both unoccupied leading to a zero Berry curvature value, only two bands in the right hand side give the finite Berry curvature as shown in Fig. 3.15 (f).

Figure 3.16 shows the number of Weyl points around the Fermi level which are presented in the BZ with the calculated AH conductivity for the series of Mn_3AN. It is shown that there are several Weyl points within the energy range -1.0 eV $<$ E $<$ 1.0 eV in all of the investigated compounds, but only Mn_3SnN and Mn_3PdN have the Weyl points within $\pm$30 meV around the Fermi level. Some

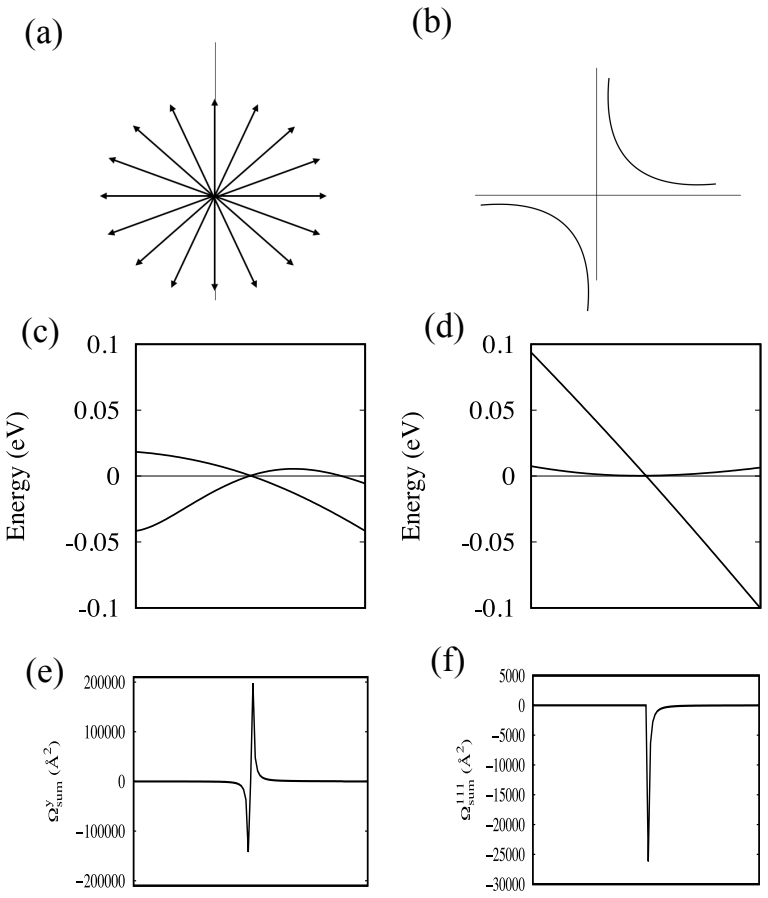

Figure 3.15: Schematic picture of Berry curvature at a lower band around a Weyl point see in (a) two dimension and (b) along one direction. Crossing bands at the Weyl point see in (c) [111] direction and (d) [010] direction. The corresponding Berry curvature at those points after taking band summation are in (e) and (f), respectively.

Table 3.5: List of Weyl points with their relative energies, chirality, and coordinate in Mn_3PtN compound.

Energy (meV)	Chirality	$k_x(2\pi/a)$	$k_y(2\pi/a)$	$k_z(2\pi/a)$
50	1	0.40	-0.26	-0.26
	-1	-0.40	0.26	0.26
	1	-0.26	0.40	-0.26
	-1	0.26	0.26	-0.40
	1	-0.26	-0.26	0.40
	-1	0.26	-0.40	0.26
-246	1	0.41	0.00	0.00
	-1	-0.41	0.00	0.00
	1	0.00	0.41	0.00
	-1	0.00	-0.41	0.00
	1	0.00	0.00	0.40
	-1	0.00	0.00	-0.40
540	1	-0.12	-0.14	-0.14
	1	-0.14	-0.14	-0.12
	1	-0.14	-0.12	-0.14
	-1	0.12	0.14	0.14
	-1	0.14	0.12	0.14
	-1	0.14	0.14	0.12
550	-1	-0.13	-0.13	-0.13
	1	0.13	0.13	0.13
560	1	-0.15	0.07	0.07
	-1	-0.07	0.15	-0.07
	1	0.07	-0.15	0.07
	-1	0.15	-0.07	-0.07
	1	0.07	0.07	-0.15
	-1	-0.07	-0.07	0.15
614	1	0.03	0.03	-0.08
	-1	-0.03	-0.03	0.08
	1	0.03	-0.08	0.03
	-1	-0.03	0.08	0.03
	1	0.08	-0.03	-0.03
	-1	0.08	0.03	0.03

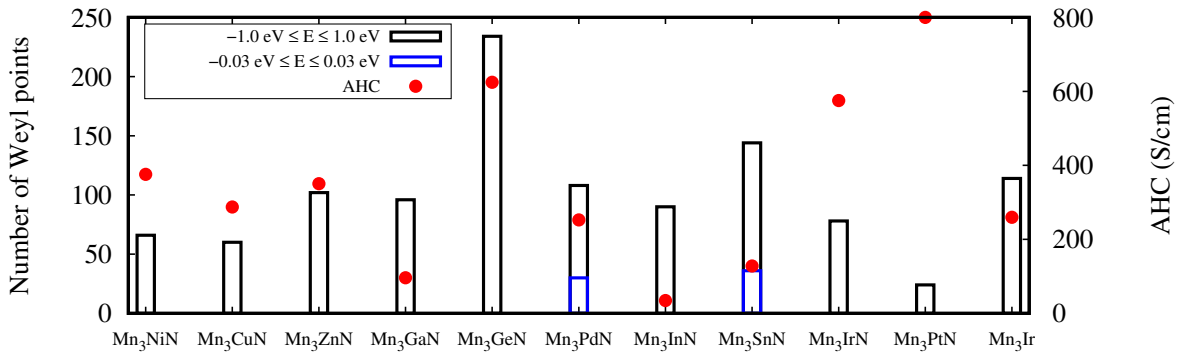

Figure 3.16: Number of Weyl points around the Fermi level (black boxes and blue boxes) with the calculated AH conductivity (red dots) for the series of Mn_3AN.

Weyl points around the Fermi level in Mn_3SnN are picked up to show the band structures around the Weyl points with its chirality and relative energy measured from the Fermi level in Fig. 3.17 (a) with the resulting Berry curvature after taking the band summation in Fig. 3.17 (b). Figure 3.17 (a) shows that the Berry curvature around Weyl points contributes to producing the sharp peaks of the band summation of the Berry curvature when the Weyl points are located near the Fermi level within the energy range of 1 meV as shown in Fig. 3.17 (b). Meanwhile, the Weyl points located at the energy more than 1meV below the Fermi energy in Fig. 3.17 (a) do not produce finite contribution of the Berry curvature after taking band summation since the crossing bands are both occupied.

Figure 3.18 and 3.19 show the contribution of the Berry curvature, classified according to its value of $\mid \Omega_n^{111}(\boldsymbol{k}) \mid$ in the first BZ, where $\Omega_n^{111}(\boldsymbol{k}) \equiv \frac{1}{\sqrt{3}}(\Omega_{yz,n}(\boldsymbol{k}) + \Omega_{zx,n}(\boldsymbol{k}) + \Omega_{xy,n}(\boldsymbol{k}))$ is the [111] Berry curvature component of band n at each $\boldsymbol{k}$ point, to the resultant AH conductivity σ_{111}. Figures 3.18 and 3.19 show the Berry curvature with small value dominantly contribute to the AH conductivity and the contribution rapidly decreases as the value becomes larger. The plot clearly shows that the contribution of the divergent Berry curvature to the AH conductivity is quite small in these AFM states even for the compounds with several Weyl points around the Fermi level leading to the divergent Berry curvature summation at the

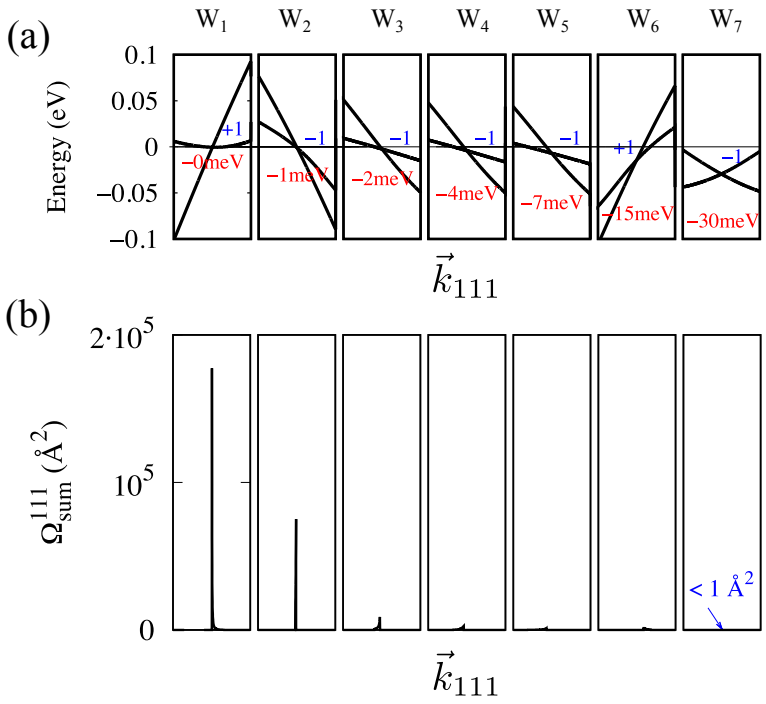

Figure 3.17: (a) Band structure and (b) Berry curvature along the [111] direction, $\vec{k}_{111}$, having Weyl points near Fermi energy in Mn_3SnN. Each panel shows an interval 0.109 (Å^{-1}) along $\vec{k}_{111}$ with Weyl point at the middle of the line. The relative energies with respect to the Weyl points are written in red, the blue number +1 and -1 indicate the chiralities of the Weyl points. The value "−0 meV" indicates the Weyl point within the energy range of -1 meV < E < 0 meV. The coordinates of these Weyl points in the reciprocal space from left to right are W_1 = (-0.06, -0.34, -0.34), W_2 = (-0.04, 0.34, 0.34), W_3 = (-0.05, 0.44, -0.16), W_4 = (-0.05, -0.16, 0.44), W_5 = (-0.16, -0.05, 0.44), W_6 = (-0.34, -0.34, 0.03) and W_7 = (-0.15, 0.47, 0.05), respectively.

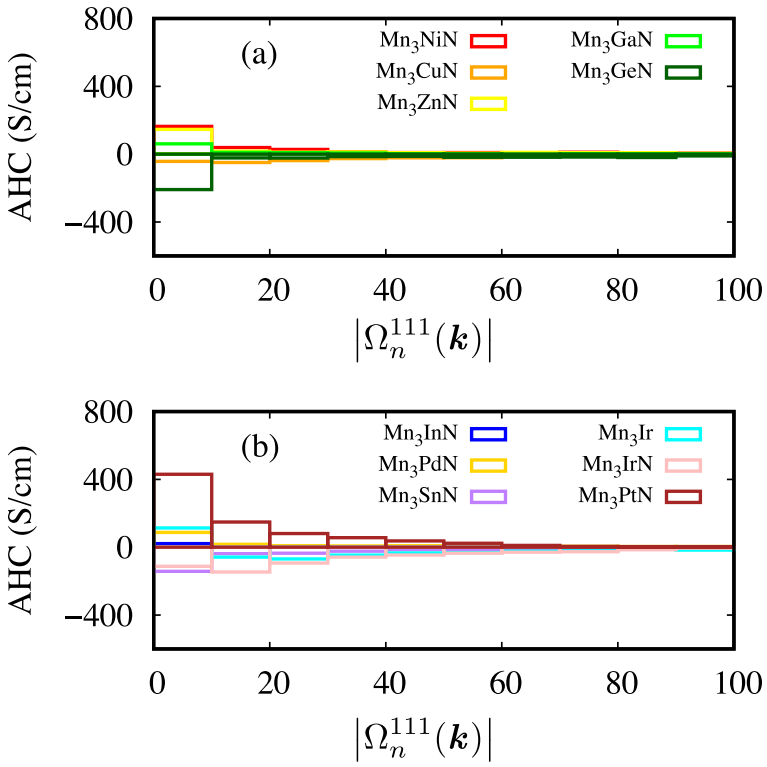

Figure 3.18: The bar chart showing contribution of the Berry curvature to the resultant AH conductivity of Mn_3AN with the A elements having (a) small and (b) large SOC. The horizontal axis is the absolute intensity of the Berry curvature.

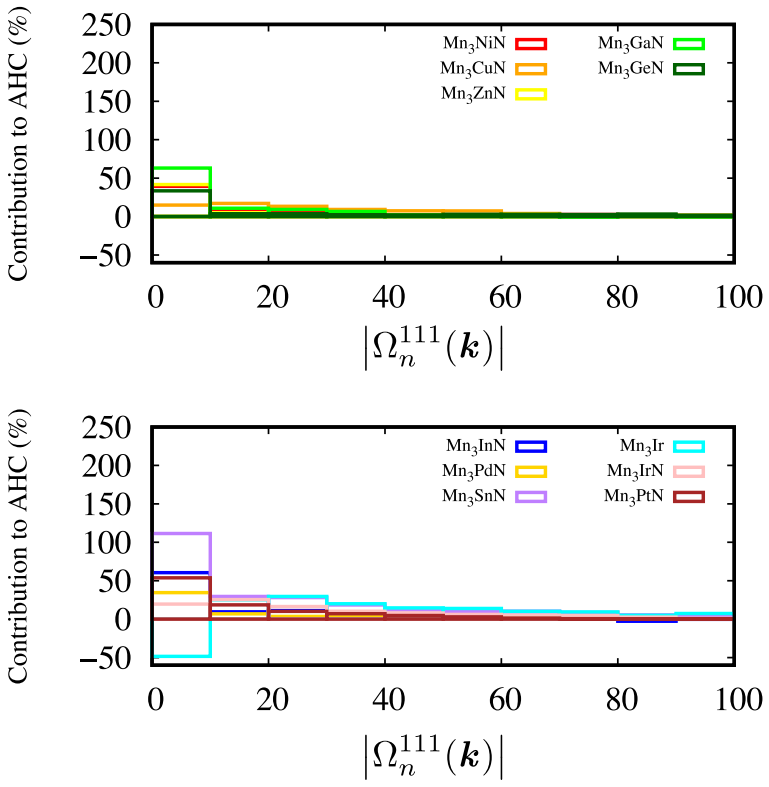

Figure 3.19: The bar chart showing percent contribution of the Berry curvature to the resultant AH conductivity of Mn_3AN with the A elements having (a) small and (b) large SOC. The horizontal axis is the absolute intensity of the Berry curvature.

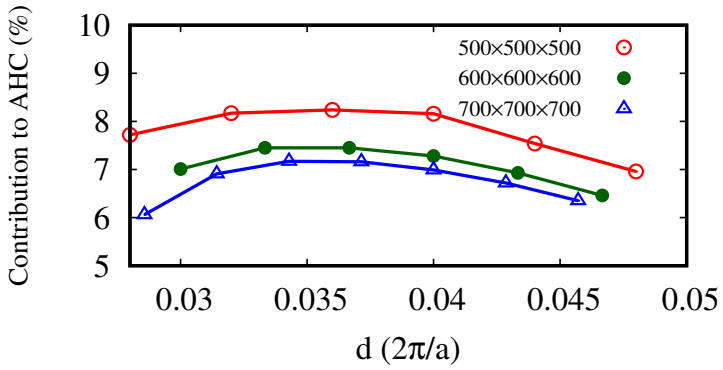

Figure 3.20: The contribution to AH conductivity from all Weyl points in Mn_3SnN as a function of the length of the edge a of cubic boxes around Weyl points. Number in the legend indicates $\boldsymbol{k}$-point mesh in which Berry curvature is integral in the first BZ.

local $\boldsymbol{k}$-region.

The contribution of the divergent Berry curvature around the Weyl points to the AH conductivity are further evaluated by calculating the $\boldsymbol{k}$-integral in Eq. 1.7 within the cubes set around each Weyl point in BZ. Decreasing the size of the cubes, the converged value of the contribution to the AH conductivity is obtained around seven percent. The small contribution of the local divergent Berry curvature to the resultant AH conductivity can be understood from too small region to produce a large contribution to the AH conductivity or from cancelling it out with the other contribution that has the opposite sign of the Berry curvature at different $\boldsymbol{k}$ points in BZ.

3.4.2 Berry curvature and spin-orbit coupling effect

The electronic structure, Berry curvature, and AH conductivity are here investigated in the Mn_3AN with A = Ni, Pd, and Pt which belong to the same group in the periodic table and are expected to have similar electronic valence states except for the effect of SOC for the purpose to discuss the topological feature

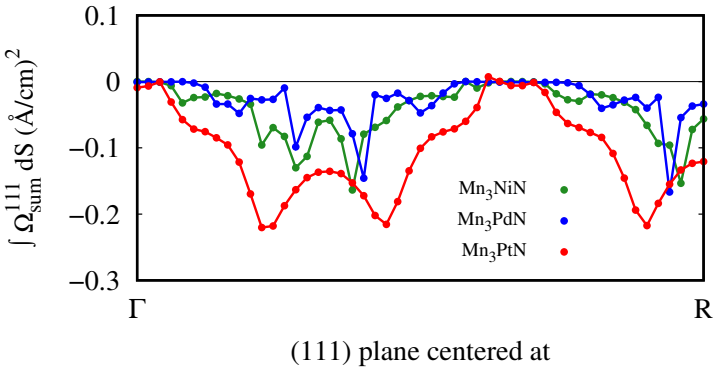

Figure 3.21: The Berry curvature integrated on the (111) hexagonal area as shown in Fig. 3.4 with its center changing from Γ to R for Mn_3AN (A= Ni, Pd, Pt).

which enhance the AH conductivity.

Figure 3.21 shows the Berry curvature integrated on the hexagonal plane with the minimum periodicity in the (111) plane, as shown in Fig. 3.4, moving the center point of the hexagonal plane from Γ to R for the three compounds. As shown Fig. 3.21, the integrated Berry curvature shows similar dependency for the (111) plane, starting from the almost zero value for the plane including Γ to the negative finite values for the one including R, for these compounds. The Berry curvature after taking band sum is shown for the (111) plane including the R point in the upper panel of Fig. 3.22, exhibiting the region with sizeable Berry curvature spread around the Fermi surfaces, which is hereinafter called active area of the Berry curvature.

Mn_3NiN and Mn_3PdN show similar values of the AH conductivity through all of the different (111) planes in Fig. 3.21. This reflects the similarity of the band structures as shown in Fig. 3.22 (d) and (e), which results in the similar Fermi surfaces and Berry curvature distribution shown in Fig. 3.22 (a) and (b). On the other hand, the small difference of the electronic structure can modify the local structure of the Berry curvature distribution as shown in Fig. 3.21 (g) and (h). In Fig. 3.22 (d) and (g), two sharp negative peaks of the Berry curvature in Mn_3NiN come from the two small gaps around the Fermi level. The SOC of Pd,

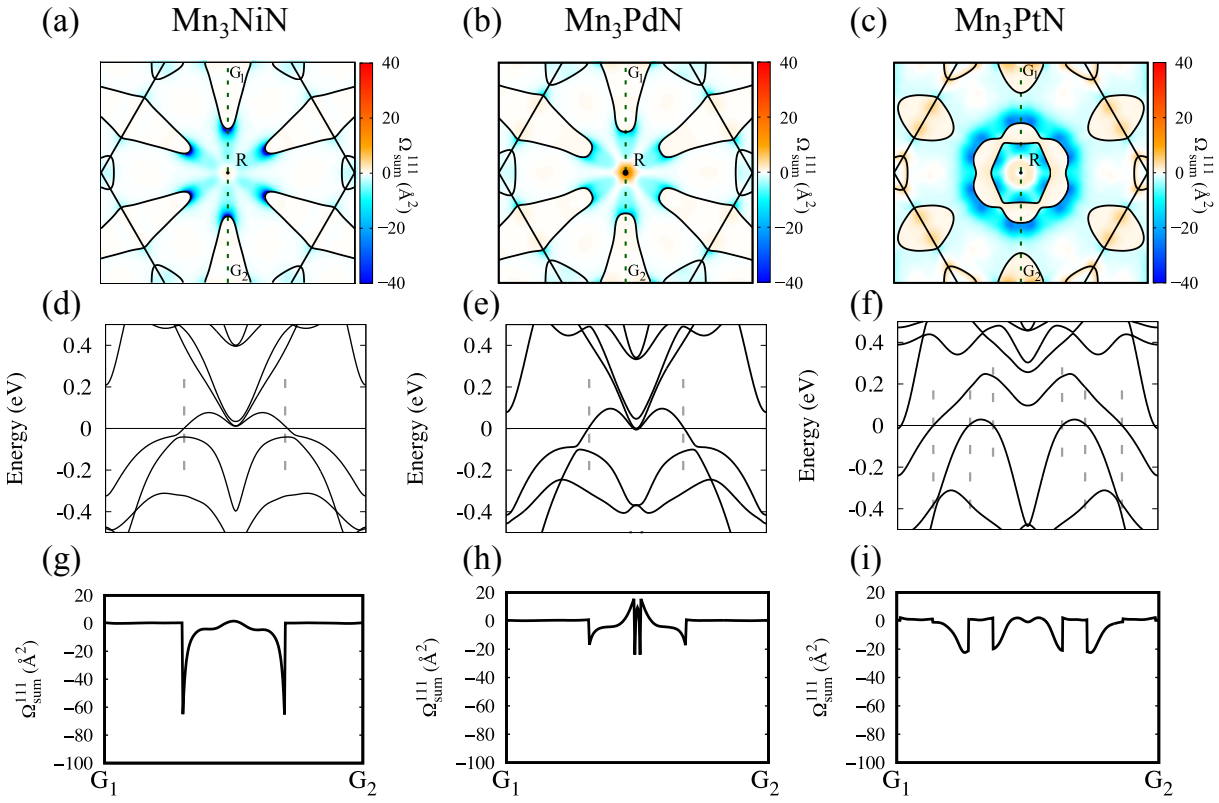

Figure 3.22: (a, b, c) Distribution of the Berry curvature after taking band summation, $\Omega^{111}_{\rm sum}$, and Fermi surfaces on the BZ plane as shown in Fig. 3.4 with its center point of R. (d, e, f) The band structure around Fermi energy and (g, h, i) Berry curvature $\Omega^{111}_{\rm sum}$ on the G_1-G_2 line shown in (a, b, c).

relatively larger than that of Ni, increases those gaps and lower the top peaks for Mn_3PdN compared to those for Mn_3NiN through the denominator of Eq. 2.39, making the possible contribution to the AH conductivity smaller than that for Mn_3NiN. Meanwhile, Mn_3PtN exhibits larger active area of the Berry curvature than those for Mn_3NiN and Mn_3PdN in its absolute value as shown in Fig. 3.22 (c). The enhancement of the Berry curvature over the BZ for Mn_3PtN, which can be seen in Fig. 3.21, is thus associated with the enlarged active area of the Berry curvature through the large SOC of Pt in Mn_3PtN and leads to the largest AH conductivity in the calculations within the three compounds.

The enhancements in the cross term of the velocity matrix in Eq. 2.39 through SOC for the states around the Fermi surfaces take place in a broad region of BZ, possibly contributing to the obtained large AH conductivity in the AFM Mn_3AN compounds.

Chapter 4

Summary

This thesis presents a comprehensive understanding about the AH effect in anti-perovskite manganese nitrides Mn_3AN. The fundamental techniques to investigate phenomena based on the first-principles calculations, Wannier interpolation, and topology analysis are shown. The stable magnetic structures, the AH effect, and the topology related to the AH effect in anti-perovskite manganese nitrides Mn_3AN are also investigated. Their magnetic octupole non-collinear AFM states, which are the most or second most stable magnetic structures whose magnetic symmetry allows to induce the AH effect, exhibit the AH conductivities comparable to those in ferromagnetic states.The thesis shows that the Berry curvatures spreading around the Fermi surfaces in the broad BZ region, resulting from the band splitting due to the SOC, dominantly contribute to the AH conductivity, while the locally divergent Berry curvatures give only a small contribution to the AH conductivity after considering the band summation and BZ integral.

This thesis opens a new viewpoint for a relation between topology and macroscopic phenomena of the AH effect in non-collinear AFM materials. Since AFM systems do not show perturbing stray field, they have many advantages and can be useful for various spintronics applications. Our study might also motivate further exciting researches in mechanisms of macroscopic phenomena associating with topology and AFM spintronic applications.

References

[1] E. H. Hall, Am. J. Math. **2**, 287 (1879).

[2] E. H. Hall, Philos. Mag. **12**, 157 (1881).

[3] N. Nagaosa, J. Sinova, S. Onoda, A. H. MacDonald, and N. P. Ong, Rev. Mod. Phys. **82**, 1539 (2010).

[4] R. Shindou and N. Nagaosa, Phys. Rev. Lett. **87**, 116801 (2001).

[5] H. Chen, Q. Niu, and A. H. MacDonald, Phys. Rev. Lett. **112**, 017205 (2014).

[6] J. Kübler and C. Felser, Europhys. Lett. **108**, 67001 (2014).

[7] Y. Zhang, Y. Sun, H. Yang, J. Železny, S. P. P. Parkin, C. Felser, and B. Yan, Phys. Rev. B **95**, 075128 (2017).

[8] S. Nakatsuji, N. Kiyohara, and T. Higo, Nature **527**, 212 (2015).

[9] N. Kiyohara, T. Tomita, and S. Nakatsuji, Phys. Rev. Appl. **5**, 064009 (2016).

[10] A. K. Nayak, J. E. Fischer, Y. Sun, B. Yan, J. Karel, A. C. Komarek, C. Shekhar, N. Kumar, W. Schnelle, J. Kübler, C. Felser, and S. S. P. Parkin, Sci. Adv. **2**, e1501870 (2016).

[11] H. Yang, Y. Sun, Y. Zhang, W.-J. Shi, S. S. P. Parkin and B. Yan, New J, Phys. **19**, 015008 (2017).

[12] M.-T. Suzuki, T. Koretsune, M. Ochi, and R. Arita, Phys. Rev. B **95**, 094406 (2017).

[13] J. Smit, Physica (Amsterdam) **21**, 877 (1955).

[14] J. Smit, Physica (Amsterdam) **24**, 39 (1958).

[15] F. Bloch, Z. Physik. **52**, 555 (1929).

[16] John David Jackson, *Classical electrodynamics*, 3rd (John Wiley and Sons, Inc.,111 River Street, Hoboken, 1998).

[17] M. V. Berry, Proc. R. Soc. London **392**, 45 (1984).

[18] R. Karplus, and J. M. Luttinger, 1954, Phys. Rev. **95**, 1154.

[19] G. Sundaram and Q. Niu, Phys. Rev. B **59**, 14915 (1999).

[20] M. P. Marder, Condensed Matter Physics (Wiley, New York) (1999).

[21] F. D. M. Haldane, Phys. Rev. Lett. **93**, 206602 (2004).

[22] X. Wang, J. R. Yates, I. Souza, and D. Vanderbilt, Phys. Rev. B **74**, 195118 (2006).

[23] T. Jungwirth, Q. Niu, and A. H. MacDonald, Phys. Rev. Lett. **88**, 207208 (2002).

[24] D. G. Martínez, I. Souza, and D. Vanderbilt, Phys. Rev. B **92**, 085138 (2015).

[25] T. Higo, D. Qu, Y. Li, C. L. Chien, Y. Otani, and S. Nakatsuji, Appl. Phys. Lett. **113**, 202402 (2018).

[26] M. Ikhlas, T. Tomita, T. Koretsune, M.-T. Suzuki, D.-N. Hamane, R. Arita, Y. Otani and S. Nakatsuji, Nat. Phys. **13**, 1085 (2017).

[27] H. Kusunose, J. Phys. Soc. Jpn. **77**, 064710 (2008).

[28] Y. Kuramoto, Prog. Theor. Phys. Suppl. **176**, 77 (2008).

[29] P. Santini, S. Carretta, G. Amoretti, R. Caciuffo, N. Magnani,and G. H. Lander, Rev. Mod. Phys. **81**, 807 (2009).

[30] M.-T. Suzuki, T. Nomoto, Y. Yanagi, S. Hayami, and R. Arita, H. Kusunose, Phys. Rev. B **99**, 174407 (2019).

[31] M.-T. Suzuki, H. Ikeda, and P. M. Oppeneer, J. Phys. Soc. Jpn. **87**, 041008 (2018).

[32] E. A. R. Assirey, Saudi Pharmaceutical Journal (May 2019).

[33] K. Suzuki and K. Kijima, Jpn. J. Appl. Phys. **44** (4A), 2081 (2005).

[34] A. K. Tagantsev, K. Vaideeswaran, S. B. Vakhrushev, A. V. Filimonov, R. G. Burkovsky, A. Shaganov, D. Andronikova, A. I. Rudskoy, A. Q. R. Baron, H. Uchiyama, D. Chernyshov, A. Bosak, Z. Ujma, K. Roleder, A. Majchrowski, J.-H. Ko, and N. Setter, Nature Communications **4**, 2229 (2013).

[35] D. J. Schroeder, A. A. Hubaud, J. T. Vaughey, Materials Research Bulletin **49**, 614 (2014).

[36] X. Lü, J. W. Howard, A. Chen, J. Zhu, S. Li, G. Wu, P. Dowden, H. Xu, Y. Zhao, and Q. Jia, Adv. Sci. **3**, 1500359 (2016).

[37] Y. Medkour, A. Roumili, L. Louail, D. Maouche, A. Saoudi, Comput. Theor. Chem, **991**, 161 (2012).

[38] B. S. Wang, P. Tong, Y. P. Sun, X. Luo, X. B. Zhu, G. Li, X. D. Zhu, S. B. Zhang, Z. R. Yang, W. H. Song, J. M. Dai, Eur. Phys. Lett. **85**, 47004 (2009).

[39] D. Fruchart, and E. F. Bertaut, J. Phys. Soc. Jpn, **44**, 3, March (1978).

[40] M. Wu, C. Wang, Y. Sun, L. Chu, J. Yan, D. Chen, Q. Huang, and J. W. Lynn, J. Appl. Phys. **114**, 123902 (2013).

[41] K. Kodama, S. Iikubo, K. Takenaka, M. Takigawa, H. Takagi, and S. Shamoto, Phys. Rev. B **81**, 224419 (2010).

[42] X. Zhou, J. P. Hanke, W. Feng, F. Li, G. Y. Guo, Y. Yao, S. Blügel, and Y. Mokrousov, Phys. Rev. B **99**, 104428 (2019).

[43] W. Shi, L. Muechler, K. Manna, Y. Zhang, K. Koepernik, R. Car, J. V. D. Brink, C. Felser, and Y. Sun, Phys. Rev. B **97**, 060406 (2018)

[44] A. A. Burkov, Nature Materials, **15**, 1145 (2016).

[45] D. R. Hartree, Math. Proc. Camb. Philos. Soc. **24**, 89 (1928).

[46] V. A. Fock, Z. Phys. **61**, 126 (1930).

[47] V. A. Fock, Z. Phys. **62**, 795 (1930).

[48] D. R. Hartree, W. Hartree, Proc. Royal Soc. Lond. A. **150**, 9 (1935).

[49] P. Hohenberg and W. Kohn, Phys. Rev. **136(3B)**, 864 (1964).

[50] J. A. White and D. M. Bird, Phys. Rev. B **50**, 4954 (1994).

[51] P. W. Ma and S. L. Dudarev, Phys. Rev. B **91**, 054420 (2015).

[52] Ph. Kurz, F. Förster, L. Nordströ m, G. Bihlmayer, and S. Blügel, Phys. Rev. B **69**, 024415 (2004).

[53] R. Singer, M. Fähnle, and G. Bihlmayer, Phys. Rev. B **71**, 214435 (2005).

[54] B. Ůjfalussy, X. D. Wang, D. M. C. Nicholson,W. A. Shelton, G. M. Stocks, Y. Wang, and B. L. Györffy, J. Appl. Phys. **85**, 4824 (1999).

[55] G. M. Stocks, B. Ůjfalussy, X. D. Wang, D. M. C. Nicholson, W. A. Shelton, Y. Wang, A. Canning, and B. L. Györffy, Philso. Mag. B **78**, 665 (1998).

[56] P. H. Dederichs, S. Blügel, R. Zeller, and H. Akai, Phys. Rev. Lett. **53**, 2512 (1984).

[57] T. Oda, A. Pasquarello, and R. Car, Phys. Rev. Lett. **80**, 16 (1998).

[58] D. D. Koelling and B. N. Harmon, J. Phys. C: Solid State Phys. **10**, 3107 (1977).

[59] C. Li, A. Freeman, H. Jansen, and C. Fu, Phys. Rev. B **42**, 5433(1990).

[60] A. Dal Corso and A. Mosca Conte, Phys. Rev. B **71**, 115106 (2005).

[61] A. Dal Corso, Phys. Rev. B **86**, 085135 (2012).

[62] A. Dal Corso, Phys. Rev. B **82**, 075116 (2010).

[63] A. Dal Corso, Comp. Material Science **95**, 337 (2014).

[64] D. R. Hamann, M. Schlüter, and C. Chiang, Phys. Rev. Lett. **43**, 1494 (1979).

[65] G. B. Bachelet, M. Schlüter, and C. Chiang, Phys. Rev. B **26**, 4199 (1982).

[66] D. Vanderbilt, Phys. Rev. B **41**, 11 (1990).

[67] J. P. Perdew, K. Burke, and M. Ernzerhof, Phys. Rev. Lett. **77**, 3865 (1996).

[68] J. C. Slater, Phys. Rev. **51** 846 (1937).

[69] O. K. Andersen, Phys. Rev. B **12**, 3060 (1975).

[70] D. D. Koelling and G. O. Arbman, J. Phys. F Met. Phys. **5**, 2041 (1975).

[71] J. Kübler, *Theory of Itinerant Electron Magnetism* (Oxford science publications, New York, 2000).

[72] P. E. Blöch, Phys. Rev. B **50**, 17952 (1994).

[73] G. Kresse and D. Joubert, Phys. Rev. B **59**, 1758 (1999).

[74] P. E. Blöch, C. J. Först, and J. Schimpl, Bulletin of Materials Science **26** (1) 33, 2003.

[75] G. H. Wannier, Phys. Rev. **52**, 191 (1937).

[76] N. Marzari, A. A. Mostofi, J. R. Yates, I. Souza, D. Vanderbilt, Rev. Mod. Phys., **84**, 1419 (2012).

[77] D. J. Thouless, M. Kohmoto, M. P. Nightingale, and M. den Nijs, Phys. Rev. Lett. **49**, 405 (1982).

[78] I. Souza, N. Marzari, and D. Vanderbilt, Phys. Rev. B **65**, 035109 (2001).

[79] P. Giannozzi, S. Baroni, N. Bonini, M. Calandra, R. Car, C. Cavazzoni, D. Ceresoli, G. L. Chiarotti, M. Cococcioni, I. Dabo, A. D. Corso, S. Gironcoli, S. Fabris, G. Fratesi, R. Gebauer, U. Gerstmann, C. Gougoussis, A. Kokalj, M. Lazzeri, L. M.-Samos, N. Marzari, F. Mauri, R. Mazzarello, S. Paolini, A. Pasquarello, L. Paulatto, C. Sbraccia1, S. Scandolo, G. Sclauzero, A. P Seitsonen, A. Smogunov, P. Umari and R. M Wentzcovitch, J. Phys. Condens. Matter **21**, 395502 (2009).

[80] G. Kresse and D. Joubert, Phys. Rev. B **59**, 1758 (1999).

[81] A. D. Corso, Comput. Mater. Sci., **95**, 337 (2014).

[82] K. Takenaka, M. Ichigo, T. Hamada, A. Ozawa, T. Shibayama, T. Inagaki, and K. Asano, Sci. Technol. Adv. Mat. **15**, 015009 (2014).

[83] Landolt-Bornstein, New Series III/19c (Springer Verlag, 1981).

[84] E. O. Chi, W. S. Kim, and N. H. Hur, Solid State Commun. **120**, 307 (2001).

[85] T. Hamada and Takenaka, J. Appl. Phys. **111**, 07A904 (2012).

[86] D. Fruchart, E.F. Bertaut, J.P. Senateur, and R. Fruchart, J. Physique Lett. **38**, 21 (1977).

[87] F. D. Murnaghan, Proc. Natl. Acad. Sci. U.S.A. **30**, 244 (1944).

[88] A. A. Mostofi, J. R. Yates, G. Pizzi, Y. S. Lee, I. Souza, D. Vanderbilt, and N. Marzari, Comput. Phys. Commun. **185**, 2309 (2014).

[89] Y. Yao, L. Kleinman, A. H. MacDonald, J. Sinova, T. Jungwirth, D.-S. Wang, E. Wang, and Q. Niu, Phys. Rev. Lett. **92**, 037204 (2004).

[90] N. Marzari and D. Vanderbilt, Phys. Rev. B **56**, 12847 (1997).

[91] X. Wang, D. Vanderbilt, J. R. Yates, and I. Souza, Phys. Rev. B **76**, 195109 (2007).

[92] D. Boldrin, I. Samathrakis, J. Zemen, A. Mihai, B. Zou, B. Esser, D. McComb, P. Petrov, H. Zhang, and L. F. Cohen, arXiv: 1902.04357v1 (2019).

[93] G. Gurung, D. F. Shao, T. R. Paudel, and E. Y. Tsymbal, Phys. Rev. Materials **3**, 044409 (2019).

[94] M. Seemann, D. Ködderitzsch, S. Wimmer, and H. Ebert. Phys. Rev. B **92**, 155138 (2015).

[95] W. Kleiner, Phys. Rev. **142**, 318 (1966).

[96] J. M. Blatt and V. F. Weisskof, *Theoretical Nuclear Physics* (Dover Publications, New York, 1991).

[97] D. A. Varshalovich, *Quantum Theory of Angular Momentum* (World Scientific, Singapore, 1988).

Appendix A

Symmetry of Berry curvature in $\boldsymbol{k}$ space

This appendix is intended to remind an general point of view about the presence of AH effect in magnetic states.

It is useful to discuss Berry curvature in $\boldsymbol{k}$ space because the Berry curvature determines the presence of the AH conductivity as shown in Eq. 1.7. The vector-form notations for the AH conductivity and Berry curvature, *i.e.*, $\sigma = (\sigma^x, \sigma^y, \sigma^z) \equiv (\sigma_{yz}, \sigma_{zx}, \sigma_{xy})$ and $\Omega_n = (\Omega_n^x, \Omega_n^y, \Omega_n^z) \equiv (\Omega_{n,yz}, \Omega_{n,zx}, \Omega_{n,xy})$ are used for convenience in discussion.

Note that the Berry curvature $\Omega_n(\boldsymbol{k})$ behaves as an axial vector in $\boldsymbol{k}$ space and it can be explained from Eq. 2.40. First, the Berry curvature is unchanged under any translation operations. Second, by rotation operations it transforms in the same way as ordinary vectors. Third, it keeps its value under the space-inversion and changes its sign by time-reversal operation. The transformation of Berry curvature under symmetry operations of magnetic point group $\bar{3}m'$ is shown in Table **??**.

In particular, systems with space-inversion symmetry hold the relation $\Omega_n(\boldsymbol{k}) = \Omega_n(-\boldsymbol{k})$ and systems with time-reversal symmetry have $\Omega_n(\boldsymbol{k}) = -\Omega_n(-\boldsymbol{k})$. Consequently, the Berry curvature is zero in whole $\boldsymbol{k}$ space, $\Omega_n(\boldsymbol{k}) = 0$.

Table A.1: The transformation of Berry curvature under symmetry operations of magnetic point group $\bar{3}m'$. The notations x, y and z are the Cartesian coordinates. $C_{n\mu}$, and m_ν indicate the n-fold rotation operator along μ axis and mirror plane corresponding with ν plane, respectively. I is the spatial inversion operator and T is the time-reversal operator. The notation $^-$ indicates anticlockwise rotation to distinguish with clockwise rotation of rotation operators without the notation.

No.	Symmetry operators	Transformation of Berry curvature
1	E	$\Omega_{[111]}(k_x, k_y, k_z) = \Omega_{[111]}(k_x, k_y, k_z)$
2	$C_{3[111]}$	$\Omega_{[111]}(k_z, k_x, k_y) = \Omega_{[111]}(k_x, k_y, k_z)$
3	$C^-_{3[111]}$	$\Omega_{[111]}(k_y, k_z, k_x) = \Omega_{[111]}(k_x, k_y, k_z)$
4	I	$\Omega_{[111]}(-k_x, -k_y, -k_z) = \Omega_{[111]}(k_x, k_y, k_z)$
5	$IC_{3[111]}$	$\Omega_{[111]}(-k_z, -k_x, -k_y) = \Omega_{[111]}(k_x, k_y, k_z)$
6	$IC^-_{3[111]}$	$\Omega_{[111]}(-k_y, -k_z, -k_x) = \Omega_{[111]}(k_x, k_y, k_z)$
7	$TC_{2[\bar{1}01]}$	$\Omega_{[111]}(k_z, k_y, k_x) = \Omega_{[111]}(k_x, k_y, k_z)$
8	$TC_{2[1\bar{1}0]}$	$\Omega_{[111]}(k_y, k_x, k_z) = \Omega_{[111]}(k_x, k_y, k_z)$
9	$TC_{2[01\bar{1}]}$	$\Omega_{[111]}(k_x, k_z, k_y) = \Omega_{[111]}(k_x, k_y, k_z)$
10	$Tm_{[\bar{1}01]}$	$\Omega_{[111]}(-k_z, -k_y, -k_x) = \Omega_{[111]}(k_x, k_y, k_z)$
11	$Tm_{2[1\bar{1}0]}$	$\Omega_{[111]}(-k_y, -k_x, -k_z) = \Omega_{[111]}(k_x, k_y, k_z)$
12	$Tm_{2[01\bar{1}]}$	$\Omega_{[111]}(-k_x, -k_z, -k_y) = \Omega_{[111]}(k_x, k_y, k_z)$

Table A.2: List of finite components of the AH effect and the corresponding required broken symmetry operations of cubic and hexagonal system. The notations x, y and z are the Cartesian coordinates. $C_{n\mu}$, and m_ν indicate the n-fold rotation operator along μ axis and mirror plane corresponding with ν plane, respectively. I is the spatial inversion operator and T is the time-reversal operator.

System	Finite components	Broken operators
Cubic	σ_{ij}	C_{nij}, IC_{nij} $(n = 2, 4)$, TC_{nij}, TIC_{nij} $(n = 0, 2, 4)$
	σ_{111}	$C_{2[1\bar{1}0]}$, $C_{2[01\bar{1}]}$, $C_{2[\bar{1}01]}$,$IC_{2[1\bar{1}0]}$, $IC_{2[01\bar{1}]}$, $IC_{2[\bar{1}01]}$ $TIC_{n[111]}$, $TIC_{n[111]}$ $(n = 0, 3)$
Hexagonal	σ_{xy}	$C_{2(xy)}$, IC_{2xy}, $TC_{2(xy)}$, TIC_{2xy} $(n = 0, 2, 3, 6)$
	σ_{yz}	C_{nz}, IC_{nz} $(n = 2, 3, 6)$, C_{2y}, IC_{2y} TC_{nz}, TIC_{nz} $(n = 0, 3, 6)$, TC_{2x}, TIC_{2x}
	σ_{zx}	C_{nz}, IC_{nz} $(n = 2, 3, 6)$, C_{2x}, IC_{2x} TC_{nz}, TIC_{nz} $(n = 0, 3, 6)$, TC_{2y}, TIC_{2y}

Therefore, the presence of magnetic symmetry in each magnetic configuration decides if the structure has finite AH conductivity. The condition of finite AH conductivity is the condition for non-vanishing Berry curvature as listed in Ref. [12, 94, 95]. It is also shown in Table A.2 for references.

Appendix B

Cluster multipole theory and multipole expansion for magnetic structures

This appendix introduces the cluster multipole theory (CMP) along with the multipole expansion for magnetic structure or so-called symmetry-adapted multipole magnetic structure that we have used in Chap. 3 to generate inequivalent magnetic structures. The theory is based on Ref. [12, 30].

In this theory, each "atomic cluster" is a set of atoms related by the crystal symmetry operators and ensured no space translation in the magnetic unit cell [12, 30]. Similar to the definition of local multipole moments for an atom [27–29], cluster multipole moment for rank-p is summation over the clusters in the magnetic unit cell:

$$M_{pq} = \frac{N^u_{atom}}{N^c_{atom}} \frac{1}{V} \sum_{\mu=1}^{N_{cluster}} M^{(\mu)}_{pq} \tag{B.1}$$

For Mn_3Ir, the unit cell contains 3 Mn atoms ($N^u_{atom} = 3$), the crystal structure contains only one atom cluster with 6 Mn atoms. For Mn_3Sn and Mn_3Ge, the unit cell contains 6 Mn atoms ($N^u_{atom} = 6$), the crystal structure contains two independent atom clusters with 6 Mn atoms in each cluster ($N^c_{atom} = 12$). The

multipole moment in the magnetic structures so-called CMP moment in the magnetic is useful to characterize for AH effect not only in ferromagnetic but also in antiferromagnetic systems [12].

It is useful to remind about the spatial distribution of magnetic vector potential in electric charge density $\rho_e(\boldsymbol{r})$ and electric current density $\boldsymbol{j}_e(\boldsymbol{r})$ given in form of multipole expansion:

$$\boldsymbol{A}(\boldsymbol{r}) = \sum_{lm} \left(b_l \boldsymbol{M}_{lm} \frac{\boldsymbol{Y}^l_{lm}(\hat{\boldsymbol{r}})}{r^{l+1}} + c_l \boldsymbol{T}_{lm} \frac{\boldsymbol{Y}^{l+1}_{lm}(\hat{\boldsymbol{r}})}{r^{l+2}} \right), \tag{B.2}$$

where $\boldsymbol{Y}^{l'}_{lm}(\hat{\boldsymbol{r}})$ is the vector spherical harmonics [27, 96, 97], $\hat{\boldsymbol{r}} = \boldsymbol{r}/r$, l is the orbital angular momentum ($l \geq 1$), $m = -l, -(l-1), .., 0, ..., l-1, l$ and $l' = l-1, l, l+1$. The expansion coefficients $\boldsymbol{M}_{lm}$ and $\boldsymbol{T}_{lm}$ are M multipole and MT multipole, respectively:

$$\boldsymbol{M}_{lm} = \sum_j \left(\frac{2\boldsymbol{l}_j}{l+1} + \boldsymbol{\sigma}_j \right) \cdot \boldsymbol{O}_{lm}(\boldsymbol{r}_j), \tag{B.3}$$

$$\boldsymbol{T}_{lm} = \sum_j \left[\frac{\boldsymbol{r}_j}{l+1} \times \left(\frac{2\boldsymbol{l}_j}{l+1} + \boldsymbol{\sigma}_j \right) \right] \cdot \boldsymbol{O}_{lm}(\boldsymbol{r}_j), \tag{B.4}$$

with

$$\boldsymbol{O}_{lm}(\boldsymbol{r}) \equiv \sqrt{\frac{4\pi}{2l+1}} \nabla [r^l Y^*_{lm}(\hat{\boldsymbol{r}})] \tag{B.5}$$

where $\boldsymbol{l}_j$ and $\boldsymbol{\sigma}_j$ are orbital and spin angular momentum of an electron at $\boldsymbol{r}_j$. A systematic procedure to generate a complete basis set for arbitrary magnetic structures was proposed in following steps [30]:

Firstly, we choose an origin magnetic structure, and determine its space group as well as Wyckoff sites of magnetic atoms. We determine a 'virtual' atomic cluster corresponding to the point group of the target crystal. Consider to magnetic moments $\boldsymbol{m}_j$ of atoms in an atomic cluster and the classify according to the irreducible representations (IREPs) of the point group, the virtual atomic cluster is set up through the symmetry adapted multipoles *i.e.* M-multipole and MT-multipole:

$$\boldsymbol{M}_{l\gamma} = \sum_{i=1}^{N_{\text{atom}}} \boldsymbol{u}^{\boldsymbol{M}}_{l\gamma i} \cdot \boldsymbol{m}_i, \tag{B.6}$$

$$\boldsymbol{T}_{l\gamma} = \sum_{i=1}^{N_{\text{atom}}} \boldsymbol{u}_{l\gamma i}^{\boldsymbol{T}} \cdot \boldsymbol{m}_i, \tag{B.7}$$

with γ runs from 1 to $2l+1$, N_{atom} is the number of magnetic atom in the atomic cluster, and $\boldsymbol{u}_{l\gamma i}^{\boldsymbol{M}} = \boldsymbol{O}_{l\gamma}(\boldsymbol{R}_i)$, $\boldsymbol{u}_{l\gamma i}^{\boldsymbol{T}} = \frac{1}{l+1}\left(\boldsymbol{O}_{l\gamma}(\boldsymbol{R}_i) \times \boldsymbol{R}_i\right)$

Secondly, we generate magnetic configuration according to M-multipoles and MT-multipoles in the virtual atomic cluster and orthonormalize the bases of multipole magnetic structures by Gram-Schmidt process. Finally, the $3N_{\text{atom}}$ orthonormalized basis set is obtained, we then can construct any magnetic configuration from this basis set.

Acknowledgements

I would love to give special thanks to my supervisor, professor Tamio Oguchi who has helped me a lot to complete my doctoral course. He always opens his heart to support people who love to study from many countries including mine. He provided me a first crucial chance to pursue the doctoral course at Osaka University as well as other opportunities to do research in our laboratory. I am sincerely grateful to my teacher, professor Yamauchi Kunihiko for many hours of enthusiastic instruction. He has provided me not only profound knowledge but also many challenges to improve my skills and obtain important research results. I warmly appreciate professor Michi-To Suzuki who always encourages me to overcome difficulties as well as gives me great support to complete my duties in my doctoral course. Sincerely thank him for his suggestion and effort to guide and help me get essential achievements. Only my effort is not enough for this work done without our teachers' enthusiastic guidance. I could not forget stimulate discussion with our laboratory teachers as well as helpful discussion with our lab-mates, Fumiaki Kuroda and other friends. I also want to give many of my thanks to Ms. Mika Asada and Ms. Chiaki Kuribayashi for their assistance in my daily life in Japan. Last, I would say thank to my family, especially, my husband and my little daughter for sharing special days with me in Japan.

Dedication

This work is dedicated to my husband and my little daughter.

List of Publications

The following paper was submited during the completion of this Ph.D.

Papers

1. Vu Thi Ngoc Huyen, Michi-To Suzuki, Kunihiko Yamauchi, and Tamio Oguchi, *"Topology analysis for anomalous Hall conductivity in the non-collinear antiferromagnetic states of Mn_3AN (A = Ni, Cu, Zn, Ga, Ge, Pd, In, Sn, Ir, Pt)"*, under review for publication in Physical Review B (arXiv:1905.07962).

Oral Presentations

1. V. T. N. Huyen, K. Yamauchi, F. Kuroda, M. -T. Suzuki, and T. Oguchi, *"Magnetic Symmetry Analysis andAb-initioCalculation of Anomalous Hall Conductivity in Co_2TiSn"*, International Conference on high performance scientific computing, Hanoi, Vietnam (March. 2018).

Poster Presentations

1. Vu Thi Ngoc Huyen, Michi-To Suzuki, Kunihiko Yamauchi, and Tamio Oguchi, *"First-principles study on anomalous Hall conductivity in non-collinear antiferromagnetic structures of anti-perovskite manganese nitrides"*, the Gordon Research Conference on Topological and Correlated Matters, Hong Kong, China (Jun. 2019).

2. Vu Thi Ngoc Huyen, Michi-To Suzuki, Kunihiko Yamauchi, and Tamio Oguchi, *"First-principles study on anomalous Hall conductivity in anti-perovskite manganese nitrides Mn_3MN (M= Ni, Cu, Ga, Ge, In, Sn, Ir) with antiferromagnetic structures"*, International annual Workshop of Center for Spintronics Research Network (CSRN), Osaka, Japan (Dec. 2018).